On the Use of LES and 3D Empirical Mode Decomposition for Analyzing Cycle-to-Cycle Variations of In-Cylinder Tumbling Flow

Zhihao Ding, Karine Truffin, Stéphane Jay, Marius Schmidt, Fabrice Foucher, Jacques Borée

On the use of LES and 3D empirical mode decomposition for analyzing cycle-to-cycle variations of in-cylinder tumbling flow

Zhihao Ding[1,2], Karine Truffin[1*], Stéphane Jay[1], Marius Schmidt[3], Fabrice Foucher[2] and Jacques Borée[4]

[1*]IFP Energies nouvelles, Institut Carnot IFPEN Transports Energie, 1-4 avenue de Bois-Préau, Rueil-Malmaison, 92852, France.
[2]Laboratoire PRISME, Université d'Orléans, 8 Rue Léonard de Vinci, Orléans, 45072, France.
[3]Reaktive Strömungen und Messtechnik, Technical University of Darmstadt, Otto-Berndt-Straße 3, Darmstadt, 64287, Germany.
[4]Institut Pprime, CNRS-ENSMA-Université de Poitiers, Téléport 2, 1 Avenue Clément Ader, Futuroscope-Chasseneuil, 86360, France.

*Corresponding author(s). E-mail(s): karine.truffin@ifpen.fr;
Contributing authors: zhihao.ding1993@outlook.com;
stephane.jay@ifpen.fr; schmidt@rsm.tu-darmstadt.de;
fabrice.foucher@univ-orleans.fr; jacques.boree@ensma.fr;

Abstract

Multi-cycle large-eddy simulation (LES) is performed to investigate cycle-to-cycle variations (CCV) of in-cylinder flow in a single-cylinder spark ignition optically-accessible research engine under motored conditions. The bivariate 2D empirical mode decomposition (EMD) is improved regarding the mode combination and computational efficiency of handling LES data. For the first time, the EMD is extended for trivariate 3D data and is applied to 3D in-cylinder flow fields to investigate large-scale flow structures and turbulence. The bivariate 2D EMD is applied to velocity fields in the central tumble plane obtained from LES to separate turbulent fluctuations from large-scale organized motions,

and regions of significant CCV are identified for different instants during intake and compression strokes. The energy transfer analysis shows that the contribution of CCV to the fluctuating kinetic energy is dominant compared to that of turbulence. The characterization of the tumble vortex in 3D is made by a vortex detection approach and the 3D EMD. The shape and rotation intensity of the tumble are evaluated, and results show that a tumble deformation occurs mainly during the second half of compression stroke, strongly contributing to CCV. The flow field is decomposed by the trivariate 3D EMD, which allows the quantification of kinetic energy contained in large and small-scale structures inside the cylinder. The local turbulent energy surrounding the spark plug is found to be partially related to the tumble motion intensity, especially in the central region. An attempt is made to link flow features extracted from 2D and 3D analyses, showing that the tumble ratio computed in the 2D tumble plane can be used to quantify the tumble deformation in 3D but is not representative of the in-cylinder kinetic energy of the large-scale tumble motion and small eddies.

Keywords: In-cylinder flow, Cycle-to-cycle variability, Empirical mode decomposition, Large eddy simulation, Turbulence, Large-scale structures

Statements and Declarations

This work was granted access to the HPC resources of TGCC under allocation Number A0082B10763 from the GENCI (Grand Equipement National de Calcul Intensif) eDARI program. Marius Schmidt kindly acknowledges generous support by Deutsche Forschungsgemeinschaft through SFB/Transregio 150 Project Number 237267381-TRR150. The authors have no relevant financial or non-financial interests to disclose. Zhihao Ding performed simulations. Marius Schmidt organized the experimental database. Fabrice Foucher helped in the analysis of experimental results. Zhihao Ding wrote the first draft of the manuscript and all authors commented on previous versions of the manuscript. Zhihao Ding, Karine Truffin and Stéphane Jay performed the physical analysis and interpretation of the results. Jacques Borée provided help and ideas in performing analysis and interpreting the results. All authors contributed to the manuscript revision, read and approved the submitted version.

1 Introduction

In spark-ignition (SI) engines, the known phenomenon denoted as cycle-to-cycle variations (CCV) is referred to as the non-repeatability of the combustion process between consecutive engine cycles, even under stationary operating conditions. CCV are undesired in SI engines as they lead to higher fuel consumption and exhaust emission as well as lower thermal efficiency, and are considered as one of the major obstacles in the efficiency improvement of SI

engines. The reduction of CCV could result in a 10% improvement in fuel consumption (Ozdor et al 1994). Therefore, the necessity to understand the origins of CCV becomes the priority in SI engine research.

In some pioneering studies (Ozdor et al 1994; Heywood 2018; Young 1981), several causes of CCV were pointed out and can be summarized into the following cyclic variations: spark discharge, in-cylinder mixture formation, and flow field. Variations in the flow field have been pointed out as the most important one among all the CCV factors (Heywood 2018). Indeed the in-cylinder mean flow and turbulent fluctuations both strongly affect thermal transport, fuel-air preparation, ignition behavior, flame propagation, and species transport. For SI engines, generating a large-scale, rotational flow motion (known as tumble) is of great importance. The large-scale tumble motion stores kinetic energy injected into the cylinder by valve jets during the intake stroke. During compression, kinetic energy in large-scale tumble motion is gradually released to small-scale structures due to the tumble breakdown (Toledo et al 2007; Borée and Miles 2014) before ignition near to top dead center (TDC). Variations in the formation and the breakdown of tumble motion can thus surely lead to CCV in the combustion process.

Further studies on CCV continue using both experimental and numerical approaches. The recent development of optical diagnostic techniques such as particle image velocimetry (PIV) offers a powerful tool to investigate the in-cylinder flow field. Nonetheless, PIV techniques are limited in a 2D vision and more suitable for multi-plane analysis, though techniques like tomographic PIV (TPIV) have been developed to capture 3D flow behavior but are applied in few in-cylinder flow analyses (Zentgraf et al 2016). A great improvement to CCV studies is achieved by the usage of computational fluid dynamics (CFD) simulations which provide a 3D description of the in-cylinder flow and mixture. The Reynolds-averaged Navier–Stokes (RANS) approach is not capable to capture CCV correctly since unsteady phenomena like turbulence are modeled (Haworth 1999). The Large-Eddy Simulation(LES) approach outplays RANS by resolving turbulent scales larger than grid size and thus allows also all the related phenomena such as air-fuel mixing, ignition, and flame propagation to be better captured. Despite its dramatic computational cost, The Direct Numerical Simulation (DNS) approach has also been introduced in SI engine modeling (Mandanis et al 2018) for a more fundamental understanding of in-cylinder flow evolution and improving LES wall models. Since its first applications in engine simulations (Naitoh et al 1992; Yavuz 2000; Thobois et al 2007; Vermorel et al 2007), LES has become the most commonly used numerical tool for CCV analysis.

A series of studies focus on investigating potential CCV sources impacting the combustion process. Different factors including geometry (Freudenhammer et al 2015; Bode et al 2019; Fontanesi et al 2015; Nicollet et al 2017), injection (Goryntsev et al 2009; Stiehl et al 2016; Schmitt et al 2015), temperature (Koch et al 2014; Ghaderi Masouleh et al 2018; Wadekar et al 2019) and mixture composition (Sjerić et al 2015; Fontanesi et al 2015; Zhao et al 2018)

were investigated. Most studies focus on the impact of in-cylinder flow on combustion, both in terms of local flow behavior near the spark plug (Enaux et al 2011; Granet et al 2012; Truffin et al 2015; Zhao et al 2018; Wadekar et al 2019) and overall characteristics at different crank angle phases (Koch et al 2014; Stiehl et al 2016; Matsuda et al 2017; Krüger et al 2017; Nicollet 2019). The large-scale tumble motion is highlighted as an important CCV factor and impacts collectively the combustion process with other potential CCV factors mentioned above. All these factors result in flow variations but do not necessarily contribute only to turbulent fluctuations but also to large-scale structures. A triple decomposition of the velocity field $U(\theta, i)$ in the case of in-cylinder flow at phase θ of cycle i is proposed in Heywood (2018) as presented below:

$$U(\theta, i) = U_{EA}(\theta) + u^c(\theta, i) + u^r(\theta, i) \tag{1}$$

The right-hand side terms designate respectively the ensemble-averaged velocity $U_{EA}(\theta)$, the CCV of large-scale motions $u^c(\theta, i)$, and the turbulent fluctuations $u^r(\theta, i)$. Such decomposition allows us to distinguish variations in both large- and small-scale structures, explore separately their evolution during an engine cycle, and quantify their impact on the combustion process.

To realize the above decomposition, Matsuda et al (2017) applied the Gaussian filter method to instantaneous velocity fields to reduce the turbulent part, and the filter size was chosen to contain 80% of the energy of the measured velocity such that only large-scale structures are retained. Some attempts have been done using fast Fourier transform (FFT) (Funk et al 2002; Joo et al 2004), but the determination of a cut-off frequency to separate large- and small-scale remains difficult. The proper orthogonal decomposition (POD) (Anindya 2000) is another common technique and a powerful tool to analyze data. It was introduced in the turbulent flow analysis by Lumley (1967). For in-cylinder flow application, POD is employed to decompose the flow field into a series of modes based on which coherent structures in turbulent flow can be identified and extracted. Graftieaux et al (2001) used POD to separate fluctuations attributed to the large-scale swirl flow from fluctuations related to small-scale turbulence. Voisine et al (2011) applied POD to in-cylinder flow fields measured by PIV to study the tumble breakdown. Several analyses can be found in the literature (Fogleman et al 2004; Liu and Haworth 2011; Liu et al 2013; Chen et al 2012) based on the phase-dependent POD performed with a snapshot method introduced by Sirovich (1987a,b,c). Buhl et al (2016) proposed the conditional averaging method. Roudnitzky et al (2006) proposed the POD triple decomposition method, and Qin et al (2014) proposed quadruple decomposition, using a specific determination of mode index based on which different parts of the flow are constructed. Chen et al (2012) proposed a practical guide for the use of POD in in-cylinder flow analysis. A new method named empirical mode decomposition (EMD) was proposed by Sadeghi et al (2019, 2021) as a promising tool to differentiate between large- and small-scale variations of the flow. Created by Huang et al (1998) to deal with time series, EMD has been extended to analyze velocity fields. Agostini and Leschziner (2014) applied a

monovariate bidimensional EMD method to the near-wall flow analysis to separate large- and small-scale structures in the fields. The velocity components were treated independently with a fixed number of IMFs based on a preliminary analysis. This decomposition was then used to study the relation between the near-wall small-scale turbulence and large-scale outer structures, concerning the response of small-scale turbulence to large-scale motions (Agostini and Leschziner 2016) and the impact of large-scale motions and small-scale turbulence on the skin friction (Agostini and Leschziner 2018, 2019). They also noticed that the separation of large- and small-scale structures was rather subjective and the choice could be difficult in case of more complex flows containing a larger range of scales. In a more recent study (Agostini and Leschziner 2022), they proposed a data-driven methodology using Auto-Encoder to separate the large-scale from small-scale motions. The Auto-Encoder was trained to efficiently learn the most important features associated with large-scale outer-flow structures identified by EMD in a pre-selected part of the flow field and then used to extract them in other parts of the flow field. The application of EMD in in-cylinder flow was presented in studies by Sadeghi et al (2019, 2021). They showed that EMD techniques could be used to decompose the instantaneous velocity field into a limited number of modes containing structures of different scales. The combination of these modes provides a low frequency (LF) part and a high frequency (HF) part. The HF part represents the turbulent fluctuations and corresponds to $u^r(\theta, i)$ in Eq 1, while the LF part is associated with the large-scale motions. By removing the ensemble-averaged velocity $U_{EA}(\theta)$ from the LF part, one can easily get access to the variations of the large-scale motion $u^c(\theta, i)$. The widely used POD method is a statistical approach in which POD basis functions are priori calculated using ensemble-averaged velocity fields whose convergence has potential impacts on the decomposition results. In contrast, EMD is a non-statistical approach that relies only on instantaneous velocity fields and its basis functions (IMF) are derived from the data during decomposition.

In the present work, we follow the previous work of Sadeghi et al (2021) on the development and application of EMD in in-cylinder flow analysis. Some improvements to the bivariate 2D EMD are made to facilitate the massive application of the EMD on 2D velocity fields obtained from LES. The extension of EMD in 3D is also realized and is applied to the 3D in-cylinder flow field for an in-depth understanding of the in-cylinder kinetic energy distribution which can be complementary to the 2D multi-planar analysis. In addition, the developed EMD tools and the vortex detection criterion Γ_3 function are employed together to characterize the tumble motion during the whole compression stroke from the 2D tumble central plane and the 3D volume.

This article is subdivided into the following subsections: first, the development of EMD for analyzing LES results is explained in Sect. 2. The experimental setup used to acquire validation data is then briefly recalled in Sect. 3.1, followed by the description of the LES methodology used in this

work in Sect. 3.3. Next, we present the results of the application of our numerical methodology in in-cylinder flow analysis. Finally, a summary outlines the main conclusions of the work.

2 Developments of multidimensional Empirical Mode Decomposition (EMD)

2.1 2D EMD for time-varying geometry

The Empirical Mode Decomposition (EMD) is a data-driven method for the analysis of nonlinear and non-stationary signals introduced by Huang et al (1998). It decomposes a signal into a finite set of amplitude and/or frequency modulated (AM/FM) components, called intrinsic mode functions (IMFs), followed by a residual component, as shown by the exemplary application plotted in Fig. 1. During the sifting process of EMD (cf Fig. 1), the local maxima and minima are identified from the current residual $r_i[n]$ of i-th iteration to generate an envelope of minima $e_l[n]$ and maxima $e_u[n]$ using the cubic spline interpolation. The residual $r_i[n]$ is then updated by subtracting the average of the envelope $m[n]$, and this step is repeated till the residual $r_i[n]$ satisfies the definition of an IMF. The extracted IMF is then removed from the input signal, and the sifting process starts again on the remained part of the signal. The EMD stops when the residual becomes monotonic.

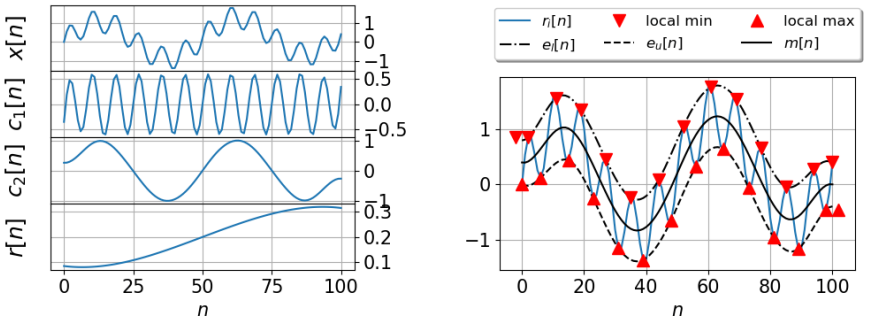

Fig. 1: Application of EMD to a 1D time series $x[n]$. IMFs $c_1[n]$, $c_2[n]$ and residual $r[n]$ are gradually extracted by EMD (left) during the sifting process (right).

EMD techniques were extended to analyze complex signals (Tanaka and Mandic 2007; Altaf et al 2007), bivariate (BEMD) (Rilling et al 2007), trivariate (TEMD) (ur Rehman and Mandic 2010) and finally more general multivariate signals (MEMD)(ur Rehman and Mandic 2011). The principle of all these approaches is based on the projection of multivariate signals into certain directions uniformly sampled over a circle (BEMD), a sphere (TEMD),

or a hypersphere (MEMD) to estimate an averaged signal envelop required by the sifting process in the EMD algorithm.

The mode mixing problem occurs during the sifting process of EMD (Huang et al 1999) and comes up also in the MEMD as the sifting process remains similar. It refers to the situation when oscillations with varying temporal scales coexist in the same IMF, or oscillations of the same temporal scale are separated into different IMFs. It is mainly caused by the intermittency with high frequency contained in large-amplitude signals (Gao et al 2008). A Noise Assisted MEMD (NA-MEMD) inspired by the ensemble EMD (EEMD) (Wu and Huang 2009) was developed by ur Rehman et al (2013) to deal with this undesired phenomenon by adding randomly generated white noise signals as additional components of the input multivariate signal to be decomposed together with the initial signal. Such a realization of EMD is repeated for NE times and the ensemble-averaged results are retained. Another improvement was made in adaptive-projection intrinsically transformed MEMD (APIT-MEMD) (Hemakom et al 2016) in which the imbalance between different components of the multivariate signal was taken into account in the sampling of projection directions. The multivariate EMD of the present study is a combination of the former two methods proposed in Sadeghi et al (2019) and noted as Ensemble NA-APIT-MEMD. It was applied to a velocity field constructed with a synthetic large-scale organized vortex and homogeneous isotropic turbulence of relatively smaller scales. The results confirmed the capability of EMD to distinguish large-scale organized motions and small-scale turbulent fluctuations based only on the instantaneous velocity field with spatial coordinates $\mathbf{x}$ at a given instant θ (representing crank angle degree in the case of in-cylinder flows or time in general cases) following:

$$U(\mathbf{x},\theta) = U_{LF}(\mathbf{x},\theta) + U_{HF}(\mathbf{x},\theta) \tag{2}$$

with $U_{LF}(\mathbf{x},\theta)$ the large-scale motion of low frequency and $U_{HF}(\mathbf{x},\theta)$ the turbulent fluctuations of high frequency.

The first application of EMD to in-cylinder flow analysis is presented by Sadeghi et al (2021) in which EMD was applied to selected in-cylinder 2D PIV velocity fields measured during the last 100 crank angle degrees (CAD) before TDC in an optically accessible research engine (Baum et al 2014). During this work, EMD was adapted to deal with complex and time-dependent geometries like the combustion chamber of a piston engine whose size changes with respect to the piston motion.

Using the methodology developed by Sadeghi et al (2021) (cf Appendix A), a 2D bivariate velocity field $U(x,y)$, organized in a regular grid, is at first decomposed along each horizontal grid row by the bivariate Ensemble NA-APIT-MEMD. The decomposition of each row is independent and is therefore parallelized: each CPU is assigned to treat a certain number of rows and results. IMFs of each row are then stored in the descending order in M horizontal pseudo IMFs noted as $\mathbf{IMF}_{Hi}$ with $i = 1, 2, ..., M$ that are shared between CPUs. The decomposition continues along each vertical grid column

of all $\mathbf{IMF}_{Hi}$ using the same parallelization strategy as in the horizontal direction. Results are then gathered in a $M \times M$ matrix of pseudo IMFs noted as $\mathbf{IMF}_{HiVj}$ with $i, j = 1, 2, ..., M$. 2D IMF modes and the 2D residual are then constructed using the combination strategy proposed in Wu and Huang (2009):

$$\mathbf{IMF}_k = \sum_{i=k}^{M} \mathbf{IMF}_{HkVi} + \sum_{j=k+1}^{M} \mathbf{IMF}_{HjVk} \tag{3}$$

where k denotes the number of 2D IMF mode with an expectation that $\mathbf{IMF}_M$ represents the 2D residual $\mathbf{r}$. The velocity field can thus be expressed as follows:

$$U(x, y) = \sum_{k=1}^{M-1} \mathbf{IMF}_k + \mathbf{r} \tag{4}$$

The number of 2D IMF modes M is determined by the direction containing less pseudo modes, *i.e* $M = \min(M_x, M_y)$ where M_x and M_y are respectively the numbers of pseudo modes in the horizontal and vertical directions. For a 1D signal of N data points, the total mode number is typically at most of the order of $\mathcal{O}(\log_2 N)$ and also depends on the complexity of the input signal. If the encountered field domain is far from being square, the number of pseudo modes in one direction may differ from the one in another direction. Even for a square field, oscillations could be more dominant in one direction than in another, which results in the same situation. Consequently, to realize the aforementioned combination strategy, it is necessary to reduce the number of pseudo modes allowed in the direction containing more pseudo modes, which leads to less physically significant modes and also incomplete decomposition in the same direction.

To overcome this problem, a solution is proposed in Sadeghi et al (2021) for the flow analysis during the last 100 CAD of compression stroke: all the velocity fields are interpolated in the direction of fewer data points (piston moving direction in this case) to achieve a square grid with the same number of data points in all directions for all crank angles. The grid resolution in the direction of fewer points varies dynamically to keep the domain size constant. Therefore, the maximal number of pseudo modes in both directions remains unchanged despite the variation in the real domain size. In this work, an improvement is made to the mode combination strategy to get rid of the interpolation step. Inspired by the fact that a simple separation to distinguish LF and HF parts of flow is sufficient, an acceleration of the EMD calculation process is also made to facilitate the extensive usage of EMD in in-cylinder flow analysis.

The new strategy is schematically presented in Fig. 2. The main difference compared to the original strategy is that the number of pseudo IMF modes in both directions is not a priori fixed. Using this strategy, different numbers of pseudo modes are allowed in both directions, for example, M in the horizontal direction and N in the vertical direction, which is often the case when the aspect ratio of the domain differs a lot from 1. All the pseudo modes are

then stored in a squared pseudo mode matrix even though it is not fully filled. To obtain the LF part of the flow field, only the last three components corresponding to the last 2D IMF and the residual in the right bottom corner of the pseudo mode matrix are needed as shown in Fig. 2, and the HF part is simply the sum of all the other pseudo modes.

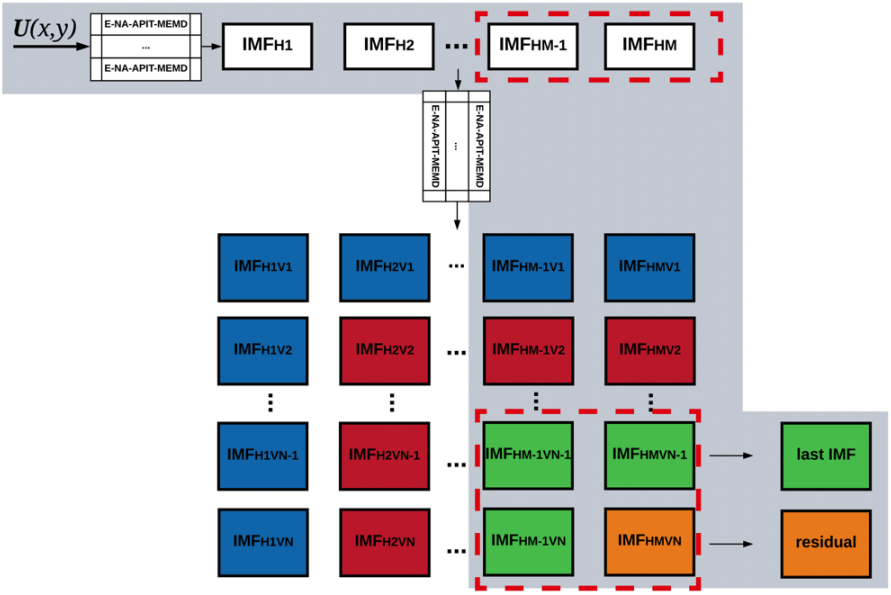

Fig. 2: Modified mode combination strategy in 2D EMD decomposition. The accelerated version is highlighted by gray background, only the last pseudo IMF and the residual is kept in the decomposition of each direction.

The interpolation of velocity fields on a grid of constant number of data points, used in the previous work by Sadeghi et al (2021) for EMD and required by other methods like POD (Fogleman et al 2004), is not necessary for the new EMD methodology. Velocity fields stored in grids of constant resolution (PIV data or LES data using Cartesian structured meshes), as shown in Fig. 3, are then directly ready to be processed by EMD. However, for unstructured or locally refined meshes, the interpolation step on a regular grid is mandatory.

The separation criterion of the LF and the HF parts is based on the energy content of each IMF as proposed in Sadeghi et al (2019, 2021) where it was demonstrated that large-scale coherent structures are stored mainly in the residual. In the current work, it was found that the residual and the last IMF provide a better reconstruction of the large-scale motions while the other IMF modes represent the vortex generation and dissipation process of smaller-scale structures, though this separation remains subjective. The lack of objective criteria for LF/HF parts separation in EMD needs further investigation. In

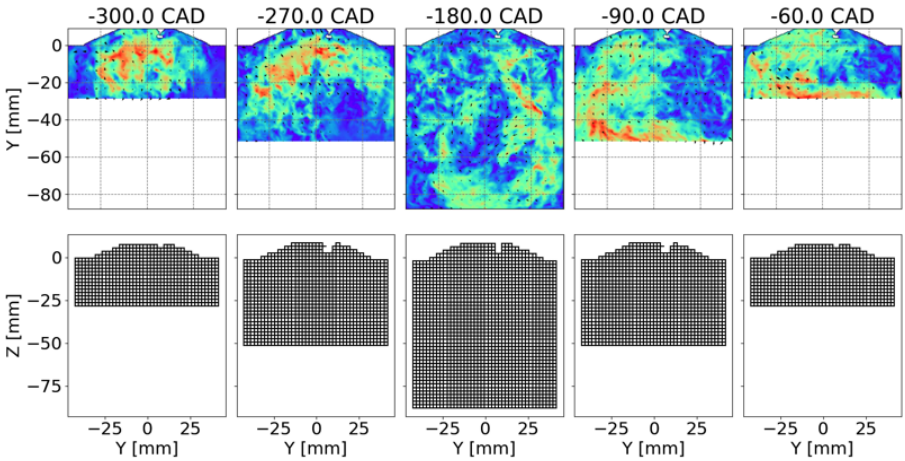

Fig. 3: Interpolation of the velocity field on uniform grids at different crank angle degrees. The grid resolution is constant, which is different from that in the previous work by Sadeghi et al (2021). Every four grid points are plotted.

previous work by Qin et al (2014, 2019) on the development of a quadruple POD method, an objective separation criterion was proposed based on the correlation between extracted modes, and is referable to the future work of EMD in in-cylinder flow analysis.

The new strategy in the present work is applied to the same velocity field used in Sadeghi et al (2021) for illustration purposes, which corresponds to a 2D instantaneous velocity field at 100 CAD before TDC measured by PIV in an optically accessible single-cylinder wall-guided engine operated at 800 rpm under motored conditions (Baum et al 2014). The LF part of the given velocity field is extracted directly by EMD and the HF part is simply the difference between the instantaneous velocity field and the LF part. Both LF and HF parts are illustrated in Fig. 4. The spark plug region is filled by values obtained using linear interpolation to avoid the discontinuity in rows and columns that the current EMD method cannot proceed with. The dimensions of the spark plug are smaller than the characteristic flow scales contained in the LF part. Furthermore, the HF part is simply deduced from the instantaneous and LF part. Therefore, linear interpolation has a negligible impact on the decomposition result. Rows of shorter length are expected in regions close to the cylinder head and NaNs are assigned to the area outside the cylinder head. The decomposition is carried out only in the domain containing real values, and each row is treated equally regardless of its length.

The same decomposition is carried out without the acceleration strategy to evaluate the speedup. The full decomposition of the velocity field gives a pseudo mode matrix of size 9×9. It is worth noting that the decomposition in the first direction (horizontal) remains the same with or without the acceleration strategy, and the acceleration is realized in the second direction (vertical).

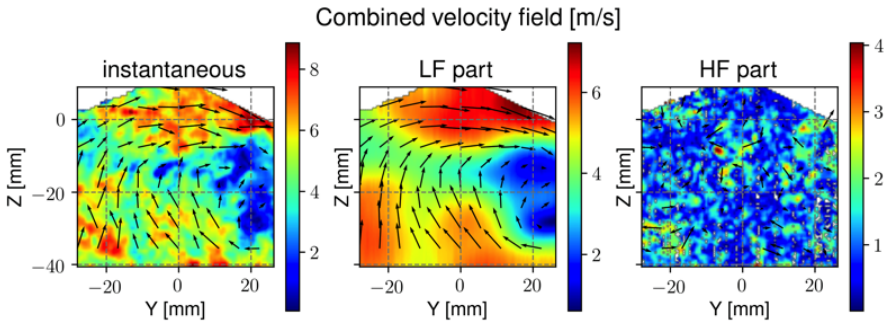

Fig. 4: Separation of large and small scales motions.

In this test case, the decomposition in the vertical direction with the acceleration is only carried out on the sum of the residual, and the last pseudo mode obtained from the decomposition in the horizontal direction, *i.e* only one 2D field. On the contrary, the decomposition in the vertical direction without the acceleration is required for all the pseudo-modes or the residual, *i.e* nine 2D fields. The theoretical gain in time in the second decomposition direction is thus equal to 9. With 108 CPUs used in both cases, our tests showed that the time used for the full decomposition is around 30.2 minutes, *i.e* 54.4 CPU hours, while that with the acceleration is 5.6 minutes, *i.e* 10.1 CPU hours. A speedup of 5.4 is obtained with the suggested acceleration strategy. Such a gain allows the extensive application of EMD in the in-cylinder flow analysis and also provides the inspiration for the extension of the EMD in 3D which will be explained in Sect 2.2.

Results obtained with the method proposed in Sadeghi et al (2021) and the present one for the LF component of the velocity field are compared in Fig. 5. The residual is also plotted for comparison. It can be noticed that including the last IMF gives a slightly better representation of the large-scale motion in some local regions, though the residual alone describes it also quite well. Qualitatively, the present methodology provides a result that seems more representative of the large-scale structure observed in the instantaneous velocity field.

The longitudinal PSD of each velocity component and their corresponding LF and HF parts are presented in Fig. 6. They are computed by using Welch's method with 50% overlapping segments. The LF part, following the evolution of the instantaneous velocity when k is small, contains energy at smaller wave numbers corresponding to large-scale structures, while the HF part is more dominant for larger wave numbers associated with small-scale turbulent structures. These two parts are clearly decoupled, indicating that the definition of the LF part as the sum of the residual and the last IMF mode is physically reasonable.

The new strategy also allows an acceleration of the current EMD. Knowing that LF contains only the last IMF and the residual, the full decomposition

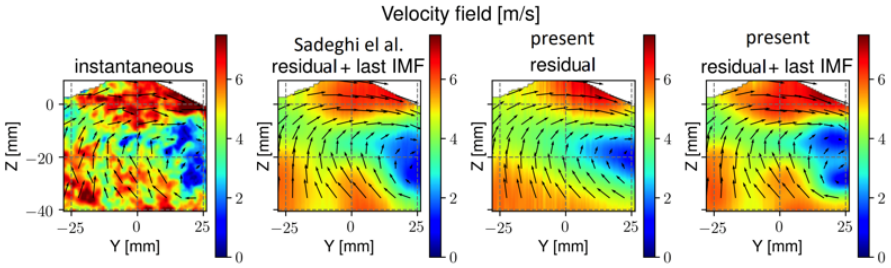

Fig. 5: Comparison of the LF part of a velocity field measured by PIV at −100 CAD using the strategy of Sadeghi et al (2021) and the strategy in the present work.

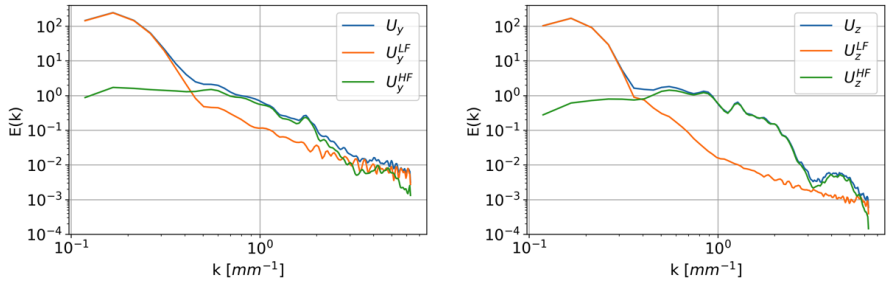

(a) U_y component. (b) U_z component.

Fig. 6: Longitudinal PSD of each component of the velocity field measured by PIV at −100 CAD and their corresponding LF and HF parts.

is not necessary if only a separation of LF/HF parts is of interest. The three pseudo modes and the residual needed to form the LF part, as shown in Fig. 2, can be obtained by a two-step decomposition highlighted by gray background: a first decomposition in the horizontal direction to obtain the residual and all the horizontal pseudo modes, and a second decomposition in the vertical direction but this time only on the residual and the last pseudo horizontal mode. A first decomposition on each line provides a pseudo residual and the last pseudo mode, which are combined before being decomposed along each column. The final LF part is the sum of the residual and the last vertical pseudo mode. The HF part is simply deduced by subtracting the LF part from the initial field. The EMD can thus be considered as a filtering method: after each decomposition, the LF part of the current decomposition is defined as the sum of the residual and the last pseudo mode of the current direction, and the next decomposition continues only the LF part of the previous one.

2.2 Spatial 3D EMD

The 2D bivariate EMD presented above shows its capacity in multi-planar analysis of in-cylinder flow. Nonetheless, the in-cylinder flow is naturally 3D, and an extension of EMD in the 3D spatial domain could help understand both large-scale motion structures and turbulence in the combustion chamber more clearly. The spatial 3D EMD deals with 3D data the same as 2D data, except that all three components of velocity are taken into account in the decomposition, and one additional dimension needs to be treated.

The procedure of spatial 3D EMD is schematically illustrated in Fig. 7 with an exemplary application to the velocity field near TDC obtained in this work. The procedure is also summarized as follows:

1. Interpolation of the input velocity field into a uniform 3D grid $U(x, y, z)$. The spark plug region is filled using linear interpolation during the decomposition.
2. Performing 1D MEMD in each row of $U(x, y, z)$ along X direction. The LF part of each row is gathered to form the LF part in X direction, noted as $U^X_{LF}(x, y, z)$.
3. Performing 1D MEMD in each row of $U^X_{LF}(x, y, z)$ along Y direction. The LF part of each row is gathered to form the LF part of $U^X_{LF}(x, y, z)$ in Y direction, noted as $U^{XY}_{LF}(x, y, z)$.
4. Performing 1D MEMD in each row of $U^{XY}_{LF}(x, y, z)$ along Z direction. The LF part of each row is gathered to form the LF part after filtering in the three directions, noted as $U_{LF}(x, y, z)$.
5. Values inside the spark plug region are masked.

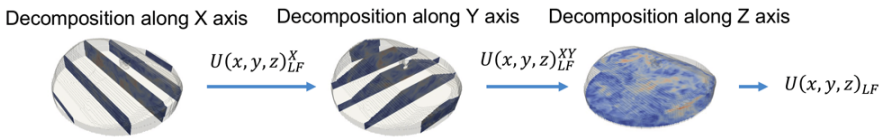

Fig. 7: Extension of EMD for the 3D velocity field.

The velocity field presented in Fig. 7 is of size $171 \times 171 \times 32$ in X, Y and Z directions. The number of pseudo modes in one direction is of the order of $\mathcal{O}(\log_2 N)$ with N the number of data points in the corresponding direction, and for the given velocity field, a total $7 \times 7 \times 5$ pseudo modes are expected. In case the full decomposition starts from the Z direction and ends in the X direction, the 3D EMD is carried out on one 3D field in the Z direction, 5 3D fields in the Y direction, and $5 \times 7 = 35$ 3D fields in X direction, while the decomposition with the acceleration methodology performs the 3D EMD on only one 3D field in each direction. The gain in time in the case of 3D applications is even more important than in 2D. The full decomposition for spatial 3D EMD is also constrained by its potential memory usage and is not

available in the current EMD tool. In the current parallel implementation of 3D EMD, each CPU has its own pseudo mode matrices for the three velocity components which are shared and updated once the decomposition is finished in a direction. Taking as an example the 3D velocity field presented in Fig. 7, the pseudo mode matrices of double-precision for the three velocity components require nearly 5.1 GB of memory per CPU. For the computing node of IFPEN equipped with an Intel Skylake G-6140 processor of 36 CPUs, the total memory demand is around 183 GB which is already close to the maximal memory available of 192 GB, though the velocity field is relatively small during the engine cycle. Such a full decomposition is then surely unfeasible for larger velocity fields close to bottom dead center (BDC).

The obtained LF and HF parts are both presented in Fig. 8. The part above $Z = 9.5$ mm is excluded during the decomposition since its irregular shape cannot be well treated by the current EMD method. Concerning the spark plug region, it should be noted that the present EMD method cannot treat signals with local discontinuity, and therefore the spark plug region is filled by values generated by linear interpolation so that no discontinuity exists as it can disturb the 1D EMD on lines passing this area. Once finished, values in the interpolation region are masked to keep the real geometry. This treatment of the spark plug region was made to make the 3D velocity field compatible with the current implementation of 3D EMD.

The interest in the HF part given by the 3D EMD is that characteristics of turbulence in the chamber can be evaluated locally and globally. The turbulence level around the spark region can impact the combustion process directly, and the EMD provides the possibility to quantify the local turbulence and evaluate its impact on flame propagation.

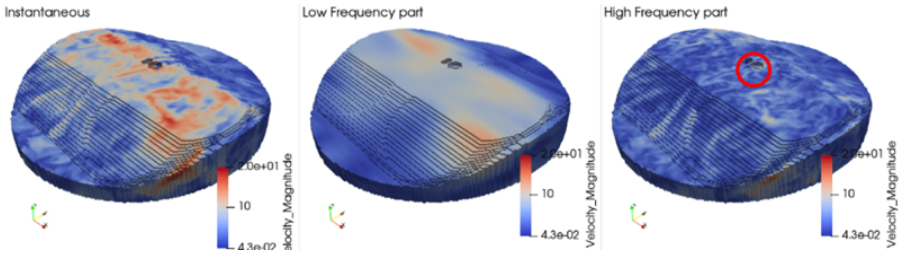

Fig. 8: Application of 3D EMD on the 3D velocity field, local turbulent energy E_k^{HF} (red circle) around spark plug is extracted.

A qualitative comparison of bivariate 2D EMD applied to a flow field in the central tumble plane and trivariate 3D EMD applied to the same flow field in the whole domain is shown in Fig. 9 in the same plane (the normal component of trivariate 3D EMD is excluded and only tangential components are compared). In 2D EMD, the third component normal to the plane is not included. From the LF part, a clear difference can be observed in the central

tumble plane where the tumble motion extracted by 3D EMD is of lower velocity magnitude in the region of $-10 < Y < 0$ mm and $Z > 0$ mm on the left part of the spark plug. The corresponding HF part obtained by 3D EMD in the same region also shows a higher level of velocity magnitude.

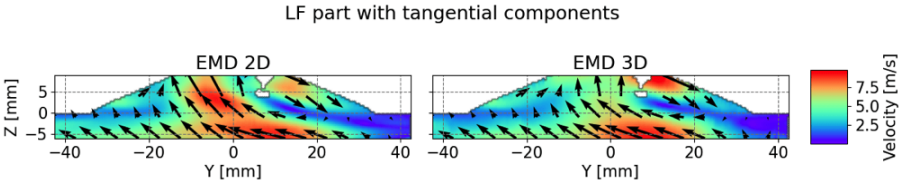

(a) LF part.

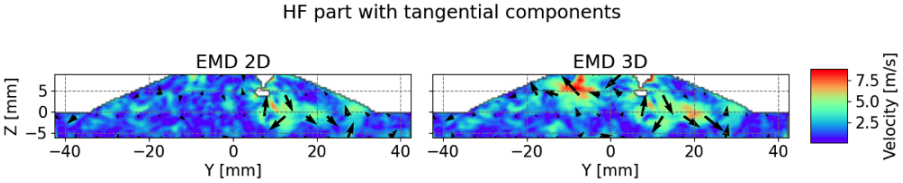

(b) HF part.

Fig. 9: Comparison of results in the tumble plane from bivariate 2D EMD and trivariate 3D EMD. only tangential components are included.

The observed difference comes from the missing third component U_x in 2D EMD. As shown in Fig. 10, a transversal motion towards the negative X direction exists on the left side of the spark plug, which indicates that the residual tumble motion is not a quasi-2D rotation around the transversal axis. The existence of the third component significantly impacts the results of EMD and especially the HF part. Knowing that the turbulence is not correctly defined in 2D with two components, the 3D EMD is recommended to quantify the turbulence despite its cost.

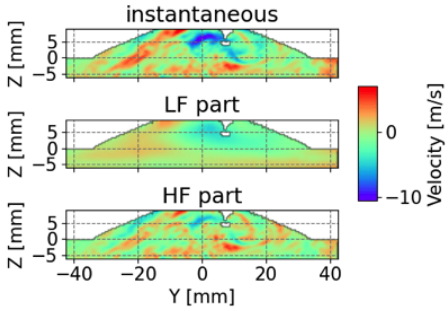

Fig. 10: Decomposition of the normal component U_x with 3D EMD.

Table 1 compares the CPU time required by bivariate 2D EMD and trivariate 3D EMD. 108 CPUs on the IFPEN supercomputer (Intel Skylake G-6140 processors) are used for both methods. The cost of bivariate 2D EMD remains reasonable for its use in analysis in 2D planes, while the trivariate 3D EMD requires much more resources comparable to LES simulations. The general use of trivariate 3D EMD, though of great interest, is still difficult. Nonetheless, the trivariate 3D EMD can still be employed to deal with some selected instants which feature important events during the engine cycle, like mid-intake, BDC, and mid-compression.

Table 1: Comparison on the computational cost of bivariate 2D EMD and trivariate 3D EMD.

CAD (deg)	-180	-22.5	-22.5
EMD type	2D	2D	3D
CPU time (CPU.hour)	29.3	10.9	558.4

3 Experimental and numerical set-up

3.1 Experimental configuration

The engine studied in this work is an optically accessible single-cylinder direct-injection four-stroke spark-ignition engine at TU Darmstadt in Germany (Baum et al 2014). The engine has two intake and two exhaust valves mounted in a pent-roof cylinder head and can be operated either with port-fuel injection (PFI) or with direct injection (DI). Optical access is enabled by a 55mm height quartz-glass liner and a flat quartz-glass piston window.

Experimental measurements are realized on two cylinder-head geometries, the wall-guided and the spray-guided configurations (Freudenhammer et al 2015). The latter one is more recent with a vast database for the validation of simulation results and therefore is selected for the present study. For the motored operation of this study, the centrally mounted injector was replaced with a dummy plug. More information on the engine can be found in Baum et al (2014). The measured pressure in intake and exhaust ports will be used as boundary conditions for the simulations.

Four engine operating points are available in this test bench, and only a single point (so-called operating point C by TU Darmstadt) has been chosen for this study. Table 2 summarizes the engine characteristics at this specific operating point.

A 2D-PIV setup was used to measure the flow in the tumble central plane located at $X = 0$ mm with Y the horizontal axis and Z the vertical axis of the plane. Two Nd:YAG cavities of a high-speed laser (Edgewave) form a light sheet of roughly 1 mm thickness, illuminating silicon oil droplets (Dow Corning Dowsil 510) seeded into the intake pipe. The Mie scattering was recorded with an SA-X2 (Photron) high-speed camera and a Sigma lens (105 mm F2.7

Table 2: Engine characteristics (0 CAD denotes top dead center (TDC) of compression stroke).

Engine speed	1500 rpm
Intake/exhaust pressure	0.95/1 bar
Intake/exhaust temperature	307/310 k
Compression ratio	8.7
Bore/stroke	86/86 mm
Connecting rod	148 mm
Displacement	499.6 cm^3
Intake valve opening	325 CAD
Intake valve closure	−125 CAD
Exhaust valve opening	105 CAD
Exhaust valve closure	−345 CAD

Macro) at a resolution of 5 CAD and processed in Davis 8.4.0 (LaVision). PIV vectors were calculated in a multi-pass of decreasing window size (64 to 32 pxl, 75% final overlap), with a peak ratio threshold of 1.3, and a universal outlier median filter to remove spurious vectors. Four measurement runs with 73 cycles each were used to calculate phase-averaged velocity fields. For further details of the used experimental setup, the reader is referred to Welch et al (2020) and Schmidt et al (2021).

3.2 Numerical studies of the TU Darmstadt engine: the state of the art

The Darmstadt engine has been widely studied involving different numerical approaches. LES is the most used numerical tool because of its capacity to capture CCV phenomena. The first LES studies were carried out by Baumann et al (2014) to validate their LES methodology by comparing results against experimental measurements. A qualitative comparison of the intake flow between two cycles was made by means of the Q-criteria, revealing an obvious variability of intake flow. Nguyen et al (2016) also performed LES but used immersed boundary method to model moving boundaries. They also investigated the sensitivity of LES results to numerical schemes and found that highly dissipative schemes can wipe the contribution of subgrid modeling and lead to a less resolved velocity field, which is undesired in the prediction of the combustion process. Janas et al (2017) carried out LES to investigate the evolution of the in-cylinder flow. The tumble shape was computed by a 2D vortex identification algorithm on a set of 2D slices throughout the cylinder and showed clear variations at mid-compression between different cycles. A modified integral length scale was also calculated to quantify the tumble size whose evolution was linked with the tumble breakdown. Wadekar et al (2019) used LES to identify CCV sources in a fired case and revealed the importance of local velocity fluctuations around the spark plug in the combustion process. DES approach was also used by Buhl et al (2017b) in the modeling of a stationary engine flow bench to study the intake flow jet. They also studied the impact of port modeling strategy on DES simulation results (Buhl et al 2018).

Iacovano et al (2022) validated their DES methodology in the simulation of operation point A of the Darmstadt engine. LBM was also developed to simulate engine flow (Haussmann et al 2020) in a flow bench configuration, and an impressive gain of 32 compared to LES in terms of computational time proved its potential in future simulation works. RANS was performed by Iacovano et al (2020) to study the mass exchange and thermal transfer in the crevice region which were stable under motored conditions. Despite its cost in the case of engine flow modeling, DNS was carried out by Impagnatiello et al (2022). Obtained DNS data was used as a reference for LES wall model development.

In this work, LES is the most suitable numerical tool since the objective is to explore the CCV of flow structures during an engine cycle. The LES methodology used in this work will be presented in the following sections.

3.3 LES methodology

3.3.1 Numerical set-up

The commercial CFD solver CONVERGE (Richards et al 2022) is used to perform consecutive multi-cycles LES as it is well designed for engine applications. It uses a finite-volume based methodology to solve the Favre-filtered equations of mass, momentum, and energy conservation. These equations are provided here for non-reactive flows:

$$\frac{\partial \bar{\rho}}{\partial t} + \frac{\partial}{\partial x_j}\left(\bar{\rho}\widetilde{u_j}\right) = 0 \tag{5}$$

$$\frac{\partial \bar{\rho}\widetilde{u_i}}{\partial t} + \frac{\partial}{\partial x_j}\left(\bar{\rho}\widetilde{u_i}\widetilde{u_j}\right) = -\frac{\partial \bar{p}}{\partial x_j} + \frac{\partial}{\partial x_j}\left[\overline{\tau_{ij}} - \bar{\rho}\left(\widetilde{u_i u_j} - \widetilde{u_i}\widetilde{u_j}\right)\right] \tag{6}$$

$$\frac{\partial \bar{\rho}\widetilde{e_s}}{\partial t} + \frac{\partial\left(\bar{\rho}\widetilde{e_s}\widetilde{u_j}\right)}{\partial x_j} = -\frac{\partial}{\partial x_j}\left(\tilde{u}_j\left(\bar{p}\delta_{ij} - \bar{\tau}_{ij}\right) + \bar{q}_i + q_i^{sgs}\right) + \widetilde{\dot{Q}} \tag{7}$$

In the momentum equation Eq. 6, $\bar{p}$ is the pressure, the filtered stress tensor is approximated by $\overline{\tau_{ij}} = 2\mu(\widetilde{S}_{ij} - \frac{1}{3}\delta_{ij}\widetilde{S}_{ll})$ with μ is the dynamic viscosity and δ_{ij} is the Kronecker symbol. $\tau_{ij}^{sgs} = -\bar{\rho}\left(\widetilde{u_i u_j} - \widetilde{u_i u_j}\right)$ is the unresolved stress tensor that modeled by Sigma model (Nicoud et al 2011). In the energy equation Eq. 7, $q_i^{sgs} = \overline{\rho e_s \widetilde{u_j}} - \bar{\rho}\widetilde{e_s}\widetilde{u_j}$ represents the unresolved flux of the sensible energy e_s. $\widetilde{\dot{Q}}$ is a source term that can be attributed for instance to evaporation or heat losses at the walls. $\overline{q_i}$ is the filtered heat flux which is approximated by:

$$\overline{q_i} = -\overline{\lambda}\frac{\partial \widetilde{T}}{\partial x_j} + \bar{\rho}\sum_k D_k \widetilde{h}_{s,k}\frac{\partial \widetilde{Y}_k}{\partial x_j} \tag{8}$$

where D_k is the species diffusion coefficient and $\widetilde{Y}_k$ the mass fraction of species k.

The CONVERGE-CFD solver (Richards et al 2022) allows a fully automatic generation of orthogonal structured grids, and the mesh generation is done at run time using a triangulated surface constructed from the engine

geometry. A second-order central difference scheme is used for spatial discretization and a second-order semi-implicit scheme for temporal integration. A step flux limiter is used for shock wave treatment (Richards et al 2017). PISO algorithm (Issa 1986) is chosen as the time integration method in time-dependent flows like the one in a piston engine. The parallelization of the solver is performed using the partitioning tool ParMetis (Karypis et al 1997) for optimal load balancing. The set of numerical parameters used in LES is summarized in Table 3. The wall-resolved LES is quite expensive as it requires a well-refined mesh on boundaries to resolve boundary layers. For this reason, wall models of velocity and temperature (Ding et al 2021) are preferred in the present study (wall-modeled LES) except for walls around intake valves where flow separation and detachment occur frequently and are thus treated by no-slip condition.

Table 3: Numerical set-up for Darmstadt engine simulation under motored conditions.

Velocity-pressure coupling	PISO (Issa 1986)
Temporal scheme	Semi-Implicit 2^{nd} order
Spatial scheme	Central scheme 2^{nd} order
Convective CFL	$u\frac{\Delta t}{\Delta x} \leq 1$
Fourier number	$\nu\frac{\Delta t}{\Delta x^2} \leq 2$
Acoustic CFL	$c\frac{\Delta t}{\Delta x} \leq 10$
SGS turbulence model	Sigma (Nicoud et al 2011)
Velocity wall modeling	Log-Law/no-slip
Temperature wall modeling	O'Rourke and Amsden (Amsden 1997)/no-slip

3.3.2 Mesh

A Cartesian cut-cell based automatic meshing approach coupled with Adaptive Mesh Refinement is used.

During the full engine cycle, the mesh size at different parts varies to well capture important phenomena during intake and compression strokes and save computational cost during the expansion and exhaust strokes which are less important in motored conditions. Some local refinements based on the fixed embedding of different levels are also applied: in the intake port and around intake valves when valves are opening to precisely predict the intake flow and the intake jets, especially the flow separation over valves which conditions the intake jets; similar refinement is applied to exhaust valves also to better capture the backflows enter in the chambers when exhaust valves are closing. The adaptive mesh refinement (AMR) is activated to improve the accuracy of the solutions in regions requiring added precision. The unresolved subgrid velocity u' is chosen as the AMR criterion with a threshold value equal to 1 m/s. The subgrid velocity is expressed as an infinite Taylor series expansion

of the resolved velocity $\tilde{U}$ and is approximated by the first order term:

$$u_i' \cong -\alpha_{[k]} \frac{\partial^2 \tilde{U}_i}{\partial x_{[k]} \partial x_{[k]}} \tag{9}$$

where $\alpha_{[k]} = dx_{[k]}^2/24$ for a cubic cell and the brackets indicate no summation.

A general description of the mesh size is given in Table 4. With this mesh strategy, the number of cells varies between 1.2 to 6.2 million. An example of the mesh during the intake stroke is presented in Fig. 11.

Table 4: Mesh size (mm) variation during the engine cycle.

	intake	compression	power	exhaust
cylinder	0.5	0.5	1	1
intake port	1	2	2	2
intake port around valves	0.5	2	2	2
exhaust port	2	2	2	1

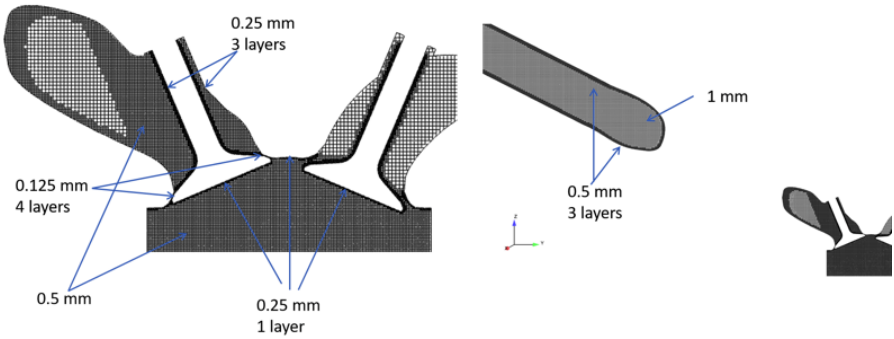

Fig. 11: Mesh topology around the combustion chamber (left) and in the intake port (right) on a cut through the valves at $X = 19$ mm. No-slip condition applied to refined mesh around valves.

3.3.3 Boundary conditions

The computational domain includes only a part of the whole test bench. It starts from the location of the second pressure sensor (closer to the cylinder) within the intake port and ends at the location of the pressure sensor within the exhaust port. A 1D simulation is performed with GT-Power to provide reference data and boundary conditions unavailable in experiments. The 1D

modeling includes the same numerical domain as in 3D LES and a three-pressure analysis is carried out: by imposing phase-averaged crank-resolved pressure traces in the intake port P_{MAN2}, in the exhaust port P_{EXH} and in the cylinder P_{cyl}, the mass exchange between different parts is calculated. A similar 1D modeling of the Darmstadt engine can be found in the work of Iacovano et al (2020). The mass flow rate computed by GT power (based on the local pressure trace P_{MAN2}) in the intake port is imposed as the inflow condition for LES in this work, on the contrary to previous LES studies on the Darmstadt engine (Nguyen et al 2016; Janas et al 2017; Wadekar et al 2019; Iacovano et al 2020) in which the phase-averaged static pressure P_{MAN2} is imposed as the total pressure of the inflow. The phase-averaged crank-resolved pressure trace measured in the exhaust port P_{EXH} is computed based on 73 experimental cycles and used as the outflow condition in the current LES. The evolution of the temperature at the same boundaries is not recorded, and only an averaged value is given. These two temperatures, T_{MAN2} and T_{EXH}, are imposed as inflow/outflow temperature. No wall temperature measurements are available and therefore T_{MAN2} and T_{EXH} are chosen as intake port wall and exhaust port wall temperature, respectively. For the cylinder part, a constant wall temperature of 333 K is imposed for all the walls including the liner and the head. A summary of prescribed boundary conditions used in the present LES study is presented in Fig. 12

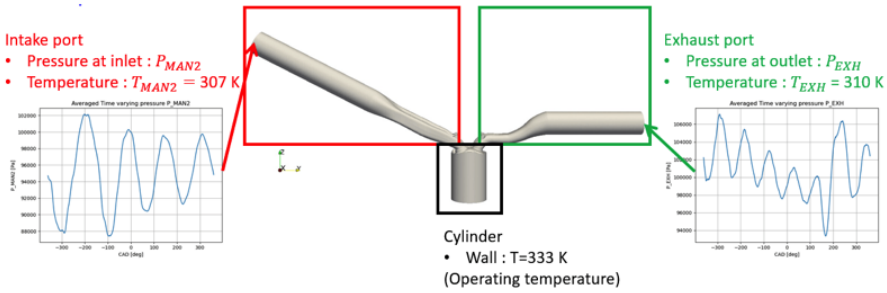

Fig. 12: Boundary conditions measured from experiments (red: intake port; green: exhaust port; black: cylinder).

A slight modification of the engine geometry is done on the crevice region of the engine as shown in Fig. 13. The real width of the crevice is 0.5 mm, which is of the order of the typical grid size used in LES. The resolution of the flow in such a narrow region is impossible without a fine discretization which would dramatically increase the computational cost. The modified crevice is two times larger in width and three times shorter so that regular LES cell size is sufficient for a minimal discretization. The annular volume at the bottom side is adjusted to keep the same compression ratio as the one measured in experiments.

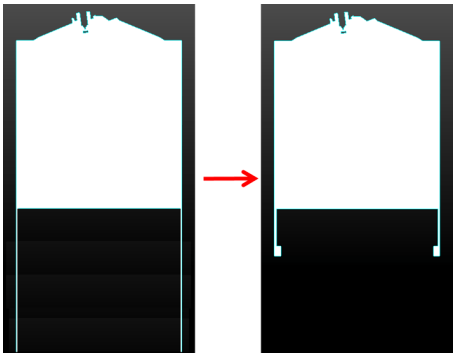

Fig. 13: Modification on the crevice region, before (left) and after (right).

In addition to the crevice description, the proper modeling of the crevice flow effects on the in-cylinder pressure evolution has been reported in previous studies (Baumann et al 2014; Janas et al 2017; Iacovano et al 2020): With the crevice included in the computational domain, the crevice flow was modeled by LES but did not allow a correct prediction of the in-cylinder pressure. This issue has also been investigated in the current work, and we propose a simple solution to couple the LES modeling with a simplified 0D crevice model to adjust the mass exchange between the chamber and the crevice:

$$\dot{m}_{cre} = \frac{m_0}{P_0} \frac{\mathrm{d}P_{cyl}}{\mathrm{d}t} \tag{10}$$

where P_0 is the initial pressure, m_0 is the estimated initial mass in the crevice used as a tuning parameter unchanged in multi-cycle simulation, and P_{cyl} is the in-cylinder pressure. The mass flow $\dot{m}_{cre}$ is taken into account in the mass, momentum, energy, and species conservation equations as a source term when it has positive values (typically during compression) and as a sink term when it has negative values (during expansion stroke). For motored conditions, Janas et al (2017) found that the overestimation of in-cylinder pressure did not impact the correct prediction of in-cylinder aerodynamics. However, it is worth noting that the current study of the motored case is part of the preliminary work for the fired case of the same engine configuration, and a correct estimation of in-cylinder thermodynamic properties including pressure and temperature is essential as thermal conditions are crucial for the combustion process.

Using the described LES methodology, the multi-cycle LES was performed using 144 CPUs on the supercomputer of CEA's Very Large Computing Centre (Intel Skylake 8168 processors). A single engine cycle costs 5760 CPU hours which corresponds to an elapsed real time of 40 hours. 27 LES cycles were calculated and the first two cycles were dropped to get rid of the influence of unrealistic initial conditions.

4 Characterization of turbulent aerodynamics in an engine

The described LES methodology is used to perform 25 consecutive LES engine cycles. Results will be validated against reference data first and then used for further analysis of the in-cylinder flow.

4.1 Validation of the LES results with experimental measurements

The thermodynamic properties obtained by LES (on one cycle) inside the cylinder are at first compared to experimental and 0D simulation results in Fig. 14. Both the in-cylinder pressure (cf Fig. 14a) and the in-cylinder trapped mass (cf Fig. 14b) match well with the reference data. Adding the crevice modeling to the numerical methodology helps to better predict the in-cylinder pressure evolution, especially in terms of its maximum value, which may be less important in motored cases but remains crucial in the fired case as the early flame propagation depends on the initial thermodynamic conditions.

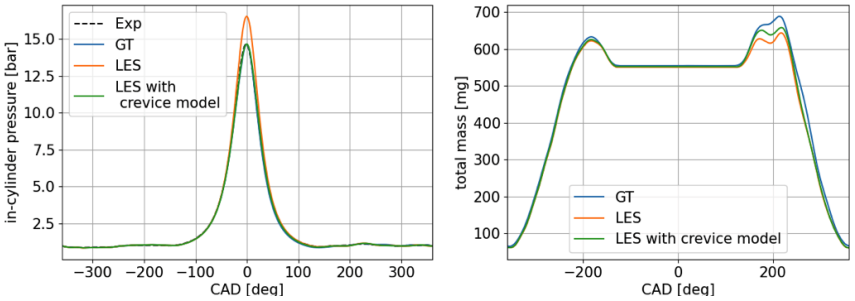

(a) In-cylinder pressure.

(b) Trapped mass.

Fig. 14: Comparison of thermodynamic properties between LES and experiments.

A quantitative comparison of the computed velocity field is then carried out. The velocity fields of 25 LES cycles are averaged and compared with that of 74 cycles from PIV measurements. The ensemble-averaged velocity field is compared in Fig. 15 in the tumble central plane at $X = 0$ mm qualitatively for instants including −300, −240, −180, −120, −90 and −60 CAD.

Fig. 15a and Fig. 15b compare the intake flow injected in the chamber during the intake phase. Both the shape and the orientation of the intake flow agree well between LES and PIV data. Fig. 15c presents the ensemble-averaged velocity field in the tumble plane at BTC. The intake flow generates a strong descending flow on the exhaust side of the chamber which is the main

source of the tumble flow. The velocity field of LES still shows some spatial fluctuations, especially in the region under the intake valves, suggesting that the phase-averaged value is statistically not fully converged. The comparison of two instants during compression is shown in Fig. 15d, Fig. 15e, and Fig. 15f. At −120 CAD, the LES seems to predict a weaker tumble front, which is the leading edge of the upward flow at the left part, while the one measured by PIV is dominant in the chamber. At −60 CAD, differences can be identified in the tumble vortex core region. Despite local differences in some instants, LES can capture most flow features.

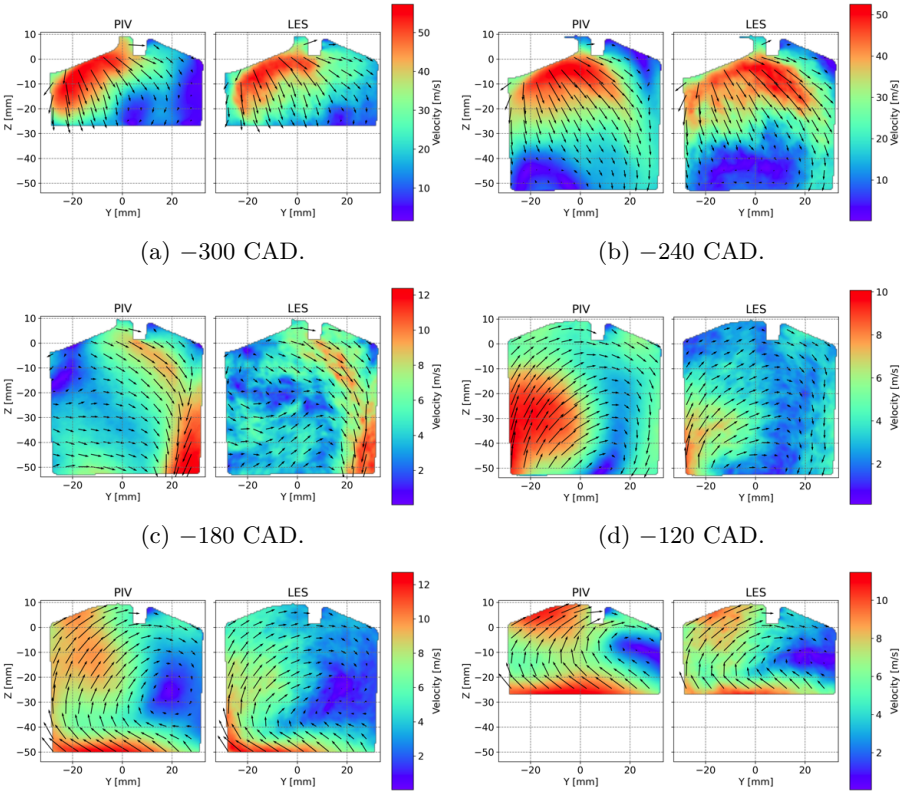

(a) −300 CAD. (b) −240 CAD.

(c) −180 CAD. (d) −120 CAD.

(e) −90 CAD. (f) −60 CAD.

Fig. 15: Comparison of the phase-averaged velocity field in the tumble plane between LES results and PIV measurements.

For a more precise comparison, the averaged velocity field is sampled over certain sampling lines in horizontal and vertical directions in the tumble plane. The comparison for crank angles -270, -180, and −90 CAD are presented in Appendix B. According to the above comparisons, the global structure of the

in-cylinder flow is properly captured, despite some differences observed locally on the two planes. Consequently, we consider that our results are in sufficient agreement with the experimental measurements so that they validate our LES methodology for the presented operating point. The next section will therefore focus on a deeper analysis of the tumble flow during compression to relate the evolution of the main flow features to the aerodynamics at spark-timing of the reactive case.

4.2 Large-scale motion and CCV

In this section, the bivariate 2D EMD is applied to the velocity fields in the central tumble plane for crank angles from −360 to 0 CAD obtained by LES. The different components of the triple and double decompositions in Eqs. 1 and 2 are extracted from the LES resolved velocity fields. For illustration, Fig. 16 presents the resulting decomposition for engine cycles 10 and 12 at −180 CAD when the organization of the flow into a rotational structure is visible.

The turbulent fluctuation U_{HF} is well separated from the instantaneous velocity field U. The LF part U_{LF} allows a more clear description of the global motion. The corresponding CCV part U_{CCV}, obtained by subtracting U_{EA} from U_{LF}, indicates regions where differences are important compared to the ensemble-averaged velocity U_{EA} in the given engine cycle. Comparing these two particular cycles, clear differences can be observed in the LF part U_{LF}: the tumble motion is more pronounced throughout the chamber in cycle 12 than in cycle 10. The corresponding CCV part U_{CCV} also indicates that compared to the averaged tumble motion of all the cycles, the tumble motion of cycle 12 differs most in the region of the tumble front.

For a more statistical description of CCV, the ensemble- (or phase-) averaged absolute value of the CCV part U_{CCV} is computed as $\overline{\|U_{CCV}(\theta)\|} = \frac{1}{N_{cycle}} \sum_{i=1}^{N_{cycle}} \|U_{CCV}(\theta, i)\|$ and presented in Fig. 17 for five different crank angles. High values of $\|U_{CCV}\|$ help identify regions with important variations in large-scale motion. The ensemble-averaged velocity U_{EA} as well as the ensemble-averaged LF part $\overline{U_{LF}}$ are also plotted in Fig. 17 to provide the flow pattern at the given instant.

U_{EA} and $\overline{U_{LF}}$ are similar, though, with a limited number of cycles, slight fluctuations still exist locally in U_{EA}. The average U magnitude varies during the engine cycle and seems to be coherent with the actual flow pattern:

- For −300 and −240 CAD during the intake stroke, CCV of the large-scale motion remains in the region where intake jets from the two valves interact with each other which results in a thick shear layer.
- At BDC, the tumble is already structured in the chamber and three regions of high CCV can be identified: the upper-right corner where a local recirculation zone is created by the intake jets; the mid-right part inside the tumble flow; the mid-left part where primary and secondary jets emerge.

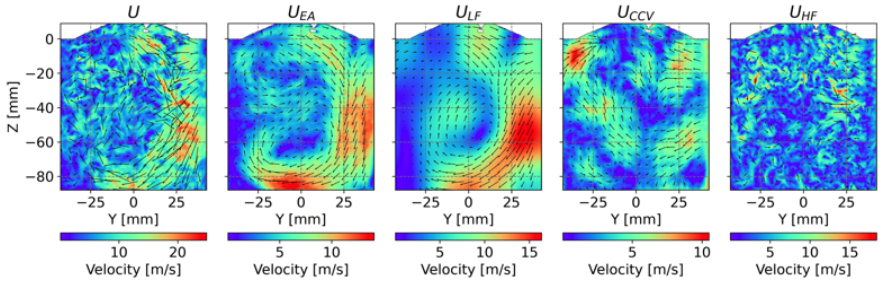

(a) cycle 10.

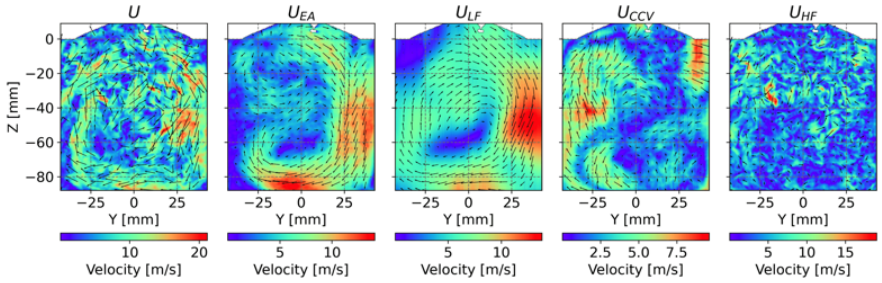

(b) cycle 12.

Fig. 16: An exemplary result of the 2D EMD for the instantaneous flow of engine cycles 10 and 12 at −180 CAD, the instantaneous velocity U is decomposed into an LF part U_{LF} containing the large-scale motion and an HF part U_{HF} representing turbulent fluctuation. CCV of the large-scale motion U_{CCV} is deduced by the subtraction of the ensemble-averaged velocity U_{EA} from LF part U_{LF}.

- At −120 CAD during compression, the flow variability is more visible on the tumble front and around the tumble rotation center. At −60 CAD, significant CCV resides inside the tumble flow which indicates that the structure of the tumble can differ significantly between different cycles when close to the end of compression.

4.3 Energy transfer between large-scale motion and small eddies

The decomposition of the flow with the 2D EMD in the tumble plane has allowed us to separate the averaged and fluctuating parts of the flow, and to distinguish the large-scale variations and turbulent fluctuations in the fluctuating part. The role of internal aerodynamics is to conserve the kinetic energy introduced by the intake jets during the intake stroke to release it in form of

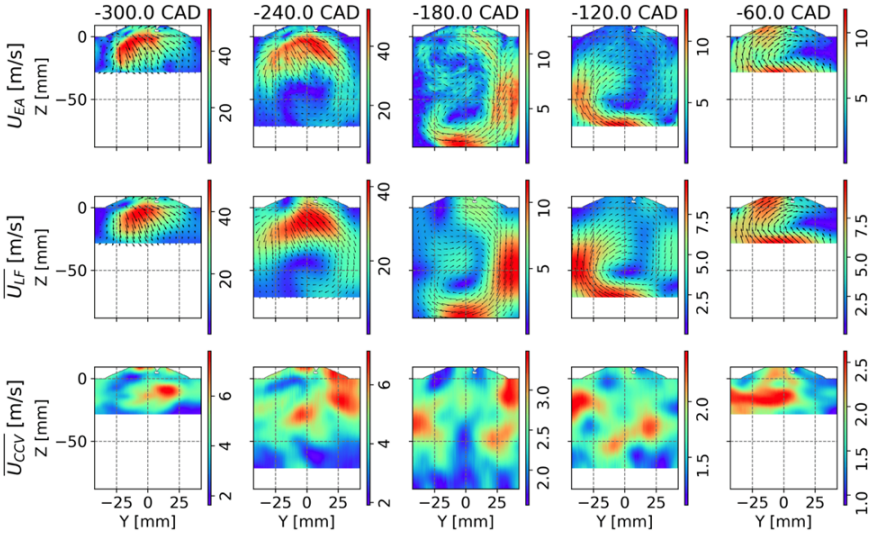

Fig. 17: Evolution of the mean flow U_{EA}, the phase-averaged LF part $\overline{U_{LF}}$ and phase-averaged CCV part $\overline{U_{CCV}}$.

turbulence at the end of compression. The energy transfer during these two phases is thus crucial and is of particular interest in this section. The following analysis focuses on the second half of compression from −100 CAD to TDC.

The instantaneous resolved velocity field can be expressed as follows using the Reynolds decomposition:

$$\tilde{U}(\theta, i) = U_{EA}(\theta) + u(\theta, i) \tag{11}$$

where $U_{EA}(\theta)$ is the ensemble-averaged resolved velocity at crank angle θ.

The kinetic energy of the ensemble-averaged resolved velocity and of its fluctuating part is computed in the tumble plane, noted as E_k^m and E_k^f respectively and defined as follows (Voisine et al 2011; Sadeghi et al 2021):

$$E_k^m(\theta) = \frac{1}{2S} \int_S \left(U_{y,EA}^2(\theta) + U_{z,EA}^2(\theta) \right) dS \tag{12}$$

$$E_k^f(\theta) = \frac{1}{2S} \int_S \left(\overline{u_y^2}(\theta) + \overline{u_z^2}(\theta) \right) dS \tag{13}$$

where $U_{y,EA}$ and $U_{z,EA}$ are ensemble-averaged resolved velocity obtained by LES, S the domain size and the fluctuating components u_y and u_z defined following:

$$u_y(\theta, i) = \tilde{U}_y(\theta, i) - U_{y,EA} \tag{14}$$

$$u_z(\theta, i) = \tilde{U}_z(\theta, i) - U_{z,EA} \tag{15}$$

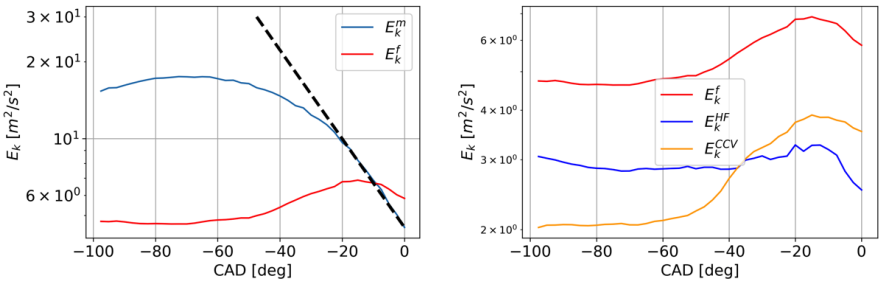

(a) The resolved kinetic energy in the mean and fluctuating part of the flow.

(b) Contribution of turbulence and CCV part in kinetic energy fluctuations.

Fig. 18: Evolution of phase-averaged resolved kinetic energy obtained from LES during the engine cycle.

The evolution of E_k^m and E_k^f during the last 100 CAD of compression is presented on a log scale in Fig. 18a. At around −70 CAD, E_k^m reaches its maximum and begins to decline. The negative slope decreases between around −70 and −20 CAD for several possible reasons: as the piston approaches TDC, the available room in the chamber reduces, and the tumbling flow is slowed down because of wall frictions. A significant increase of E_k^f can also be noticed after −50 CAD and may explain the drop of E_k^m observed during the same period: the kinetic energy is transferred from the mean flow to the fluctuating part which is usually considered as the result of tumble breakdown (Voisine et al 2011). After −20 CAD, as described by the black dashed line in Fig. 18a, E_k^m decreases exponentially with time and its evolution can be expressed as:

$$E_k^m(\theta) = E_k^m(\theta_0) e^{-\frac{t-\theta_0}{\tau_d}} \tag{16}$$

with $\theta_0 = -20$ CAD, t the time in CAD and τ_d a characteristic time scale of the decrease of E_k^m equals to 25 CAD or 2.77 ms. The turnover time scale of the tumble at −20 CAD can be estimated as $\tau_t = L/U$ where L is the available height in the chamber and U is an approximated value of the mean velocity magnitude. Taking $L = 15$ mm and $U = 5$ m/s, τ_t equals to 3 ms which is of same order as τ_d. This indicates that the rate of decay of the kinetic energy of the mean tumbling flow scales with its turnover time scale, as found by Voisine et al (2011). This is usually interpreted as the signature of tumble breakdown. During the last 10 CAD, E_k^f becomes larger than E_k^m, which means that the global motion has vanished.

Using the Reynolds decomposition, the fluctuating part obtained still contains contributions from CCV of the large-scale motion and turbulence. 2D EMD has made it possible to separate these two types of fluctuations of different scales. In Fig. 18b the evolution of the kinetic energy in CCV, E_k^{CCV}, and that of turbulence, E_k^{HF}, are plotted. The turbulent kinetic energy E_k^{HF}

remains stable during compression except for the last 10 CAD during which a decay is present as the piston reaches almost the end of displacement. E_k^{CCV} seems, therefore, to be responsible for the increase of the kinetic energy in the fluctuating part: it increases in sync with E_k^f beyond -50 CAD. After -35 CAD, a more important part of the fluctuating kinetic energy is contained in the CCV part rather than in the turbulence. The evolution of E_k^{CCV} indicates that an important change in the large-scale evolution of the flow takes place after around -50 CAD. The averaged U_{CCV} magnitude at -60 CAD presented in Fig. 17 also confirms that significant variations of the large-scale structures appear inside the tumble flow.

The application of bivariate 2D EMD on velocity fields in the central tumble plane gave us a deeper insight into the variations of the tumble motion in both large- and small-scale structures during the intake and the compression. Large-scale variations were noticed in the tumble motion, in the tumble vortex core region as well as in the tumble front region. The analysis of the energy transfer between large- and small-scales showed that in this engine configuration, the main contribution to the increase of flow variations near TDC comes from the large-scale tumble motion rather than turbulent fluctuation. The classic tumble breakdown process did take place as captured by the exponential decrease of E_k^m but quite late in the cycle, indicating the existence of residual large-scale structures near TDC.

Observations of flow variations in the central tumble plane cannot be explained using only information from the same plane as the tumble motion is naturally three-dimensional. In the next section, analysis tools for describing the tumble motion in the cylinder volume will be proposed to complete the analysis in 2D planes using EMD. The tumble ratio (Jaffri et al 1997) is evaluated for all the cycles around the tumble center detected by Γ_1 function (Graftieaux et al 2001) at -22.5 CAD which corresponds to the spark timing of the fired case at the same operating point. In Fig. 19, the distribution of the computed $\mathrm{TR}_{2D}(\theta_{ign})$ for all cycles is presented, and a clear cyclic variability can be noted. Two extreme cycles, cycle 10 and cycle 12, with opposite behavior in terms of tumble ratio, are chosen for the qualitative analysis in the 3D flow analysis.

4.4 Flow characterization in 3D

The characterization of the tumble flow is classically carried out in the tumble plane where the rotational flow is visible, especially in experimental studies as PIV measurements are usually available for 2D planes. However, analysis is limited as a complete description of the tumble is not accessible, including CCV and turbulence variations in 3D. In this section, tools including Γ_{3p} and 3D EMD are applied to the velocity fields to explore their capability to characterize the 3D tumble flow motion.

In 2D analysis, the Γ_1 and Γ_2 functions proposed in Graftieaux et al (2001) are widely used for identifying the tumble center and the vortex region in SI engine studies (Janas et al 2017; Hanuschkin et al 2021; Sadeghi et al 2021).

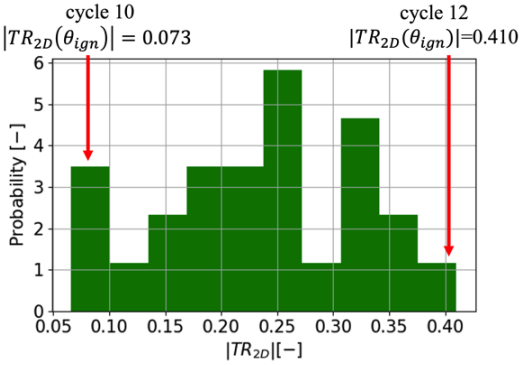

Fig. 19: Distribution of tumble ratio $\mathrm{TR}_{2\mathrm{D}}(\theta_{ign})$ at -22.5 CAD computed using U_{LF} of the tumble central plane.

For 3D rotational flows like the tumble flow, Γ_1 and Γ_2 are limited due to their 2D nature.

Some extensions were made to create a 3D Γ function (Bücker et al 2012; Janas et al 2017; Nicollet 2019), though all of them are based on the 2D Γ_1 and Γ_2 functions. An extension of Γ in 3D was applied in Gohlke et al (2008), named $\mathbf{\Gamma}_3$. It is more appropriate for strongly three-dimensional flows and was initially dedicated to external flows to identify vortical structures in a 3D volume. $\mathbf{\Gamma}_3$ was then for the first time applied to in-cylinder flow as presented in Buhl et al (2017a) with slight modifications: $\mathbf{\Gamma}_3$ was computed to obtain the rotation direction at first and then was recomputed in the rotation plane normal to the rotation direction, noted as $\mathbf{\Gamma}_{3p}$. In the present work, the $\mathbf{\Gamma}_{3p}$ was modified to be Galilean invariant so that the local convection is taken into account. It is then used to identify the tumble vortex during compression.

$\mathbf{\Gamma}_3$ is first evaluated in the volume of the combustion chamber using the following formula:

$$\mathbf{\Gamma}_3(\mathbf{x},\theta) = \frac{1}{V}\int_{\mathbf{x}_0\in V} \frac{\mathbf{r}\left(\mathbf{x}_0\right)\times\hat{\mathbf{u}}\left(\mathbf{x}_0,\theta\right)}{\left\|\mathbf{r}\left(\mathbf{x}_0\right)\right\|\left\|\hat{\mathbf{u}}\left(\mathbf{x}_0,\theta\right)\right\|} d\mathbf{x}_0 \tag{17}$$

with θ the crank angle, V a sub-volume centered at the point $\mathbf{x}$ and $\mathbf{r}\left(\mathbf{x}_0\right)$ the distance vector points from $\mathbf{x}$ to $\mathbf{x}_0$. $\hat{\mathbf{u}}\left(\mathbf{x}_0,\theta\right)$ is difference between the velocity $\mathbf{u}\left(\mathbf{x}_0,\theta\right)$ at $\mathbf{x}_0$ and the averaged local convection velocity $\langle\mathbf{u}\rangle_V(\mathbf{x},\theta)$:

$$\hat{\mathbf{u}}\left(\mathbf{x}_0,\theta\right) = \mathbf{u}\left(\mathbf{x}_0,\theta\right) - \langle\mathbf{u}\rangle_V(\mathbf{x},\theta) \tag{18}$$

$\langle\mathbf{u}\rangle_V(\mathbf{x},\theta)$ is the average velocity inside V. By taking into account the local convection, Γ_3 becomes Galilean invariant.

The computed $\mathbf{\Gamma}_3$ is a vector quantity and its orientation directly represents the rotation direction at the point $\mathbf{x}$ by a simple normalization of $\mathbf{\Gamma}_3$:

$$\mathbf{e}_{\Gamma_3}(\mathbf{x},\theta) = \frac{\mathbf{\Gamma}_3(\mathbf{x},\theta)}{\|\mathbf{\Gamma}_3(\mathbf{x},\theta)\|} \tag{19}$$

It should be noted that the result of $\mathbf{r}(\mathbf{x}_0) \times \hat{\mathbf{u}}(\mathbf{x}_0,\theta)$ may result in contribution to Γ_3 not aligned with the rotation direction $\mathbf{e}_{\Gamma_3}$, and thus reduce the value of $\|\Gamma_3\|$. To enhance the detection of local rotation, $\mathbf{\Gamma}_3$ is recomputed using velocity and distance vectors $\mathbf{u}_p(\mathbf{x}_0,\theta)$ and $\mathbf{r}_p(\mathbf{x}_0)$ projected into the rotational plane normal to the rotation direction and defined as follows:

$$\mathbf{r}_p(\mathbf{x}_o) = \mathbf{r}(\mathbf{x}_o) - \mathbf{e}_{\Gamma_3}(\mathbf{x},\theta) \cdot (\mathbf{r}(\mathbf{x}_o) \cdot \mathbf{e}_{\Gamma_3}(\mathbf{x},\theta)) \tag{20}$$

$$\mathbf{u}_p(\mathbf{x}_o,\theta) = \hat{\mathbf{u}}(\mathbf{x}_o,\theta) - \mathbf{e}_{\Gamma_3}(\mathbf{x},\theta) \cdot (\hat{\mathbf{u}}(\mathbf{x}_o,\theta) \cdot \mathbf{e}_{\Gamma_3}(\mathbf{x},\theta)) \tag{21}$$

The final formulation of $\mathbf{\Gamma}_{3p}$ is then given by:

$$\mathbf{\Gamma}_{3p}(\mathbf{x},\theta) = \frac{1}{V}\int_{\mathbf{x}_0 \in V} \frac{\mathbf{r}_p(\mathbf{x}_0) \times \mathbf{u}_p(\mathbf{x}_0,\theta)}{\|\mathbf{r}_p(\mathbf{x}_0)\| \, \|\mathbf{u}_p(\mathbf{x}_0,\theta))\|} d\mathbf{x}_0 \tag{22}$$

Compared to the definition in Buhl et al (2017a), $\mathbf{u}_p$ is used here both in the denominator and the numerator in the current study to keep a more consistent expression. The magnitude of $\mathbf{\Gamma}_{3p}$ describes quantitatively if organized rotation exists: unity values are related to perfect vortices without any deformation while small values close to zero correspond to nearly pure convection. Based on $\mathbf{\Gamma}_{3p}$, tumble centers can be determined the same way as in 2D cases: along the main axis of the tumble motion (X axis in this study), a local center can be determined where the magnitude of $\mathbf{\Gamma}_{3p}$ is maximized. All the local centers constitute a tumble center line (TCL) around which the tumble rotates as illustrated in Fig. 20.

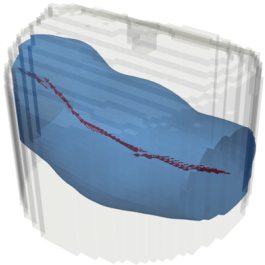

Fig. 20: Tumble vortex core identified by the isosurface of $\|\mathbf{\Gamma}_{3p}\| = 0.5$ (blue) and tumble center line (red) along X axis around which the tumble motion is organized. Local tumble center at x_0 is of maximal value of $\|\mathbf{\Gamma}_{3p}\|$ for all points at $x = x_0$.

For an application to a spark-ignition engine, the following methodology is proposed: first, interpolate the velocity field on a 3D uniform grid that includes the whole combustion chamber; then, apply the $\mathbf{\Gamma}_{3p}$ criterion to the whole chamber. In the present case, a grid resolution of 2 mm is chosen as a compromise between the computational cost and the precision. The volume V in Eq. 17 is set to be a sphere of radius R varying dynamically with the available chamber room height $H_c(\theta)$ such that $R = 0.3L$ as recommended in Gohlke et al (2008) where L is the characteristic scale of the searching structure, and in this case equals to $0.5H_c(\theta)$ assuming the tumble fills the chamber as a pure rotation. In practice, the treatment of the velocity field at BDC using 36 CPUs on the IFPEN supercomputer (Intel Skylake G-6140 processors) takes 50 minutes, which is acceptable for a massive application on a large number of engine cycles.

$\mathbf{\Gamma}_{3p}$ does not quantify the rotation intensity. For that purpose, a local tumble ratio was defined in Buhl et al (2017a) along the TCL at each center $\mathbf{x}_c$ using average local vorticity evaluated on the circular plane with a radius of 5 mm perpendicular to the TCL. This formulation ignores the flow field outside the small circular plane where most of the tumble structure resides. Therefore, in this study we propose another formulation named local rotation intensity (**RI**) which quantifies the rotation intensity of the tumble motion from all the local rotation planes:

$$\mathbf{RI}(\mathbf{x}_c, \theta) = \frac{1}{\omega_{ref}} \frac{\int_{\mathbf{x}_0 \in V_r} \mathbf{r}_p(\mathbf{x}_0) \times \rho(\mathbf{x}_0, \theta)\, \mathbf{u}_p(\mathbf{x}_0, \theta)\, d\mathbf{x}_0}{\int_{\mathbf{x}_0 \in V_r} \rho(\mathbf{x}_0, \theta) \left\|\mathbf{r}_p(\mathbf{x}_0)\right\|^2 d\mathbf{x}_0} \tag{23}$$

with V_r representing the volume including only points very close (whose normal distance to the plane is less than the typical mesh cell size 0.5 mm) to the rotational plane of the center $\mathbf{x}_c$, and ω_{ref} the engine rotation speed used for normalization. The rotational plane is defined as the plane normal to the local rotational direction passing through the local center $\mathbf{x}_c$. This formulation is quite similar to that of the global tumble ratio (Jaffri et al 1997) except that only points close to the rotational plane are used with their projected quantities and that the tumble ratio is computed around the local center instead of the global center of gravity. The **RI** vector is also the normalized angular speed of the flow around the three axes.

With the criterion $\mathbf{\Gamma}_{3p}$, the tumble center line and the corresponding local rotation intensity **RI**, we can describe precisely the tumble structure in the chamber. Their evolution during compression may provide information about the tumble deformation or breakdown.

Γ_{3p} is calculated for several CADs of compression stroke during which the large-scale tumble motion is well-formed at BDC and interacts with the piston and the cylinder walls up towards TDC.

An exemplary result of Γ_{3p} applied to two engine cycles at -22.5 CAD, which corresponds to the ignition timing of the reactive case, is presented in

Fig. 21. With a threshold of Γ_{3p}=0.5 as proposed in Gohlke et al (2008), the core part of the tumble can be visualized.

For the given two engine cycles, the structure of the flow behaves completely differently. In cycle 12, the rotational structure has a cylindrical shape which is typical of an ideal tumble motion, while in cycle 10, two vortex cores are emphasized. The associated vector fields of Γ_{3p} plotted in Fig. 21 provide an insight into the global structure of the flow: as indicated by red arrows, the rotation in cycle 12 is mainly along the X axis, while in cycle 10 a pair of counter-rotating vortices appears and tends to rotate around an inclined axis in YZ plane.

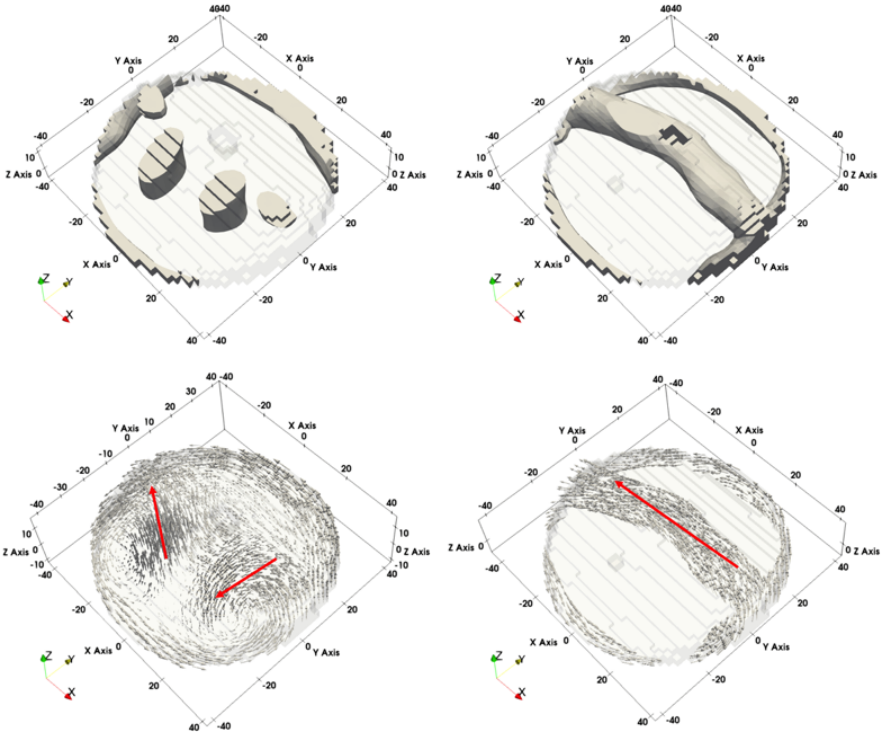

Fig. 21: An exemplary result of the Γ_{3p}: iso-surface of $\|\mathbf{\Gamma}_{3p}\| = 0.5$ (top) and vector field of Γ_{3p} (bottom), for the instantaneous flow of engine cycles 10 (left) and 12 (right) at -22.5 CAD.

The differences in the tumble can be observed even earlier during the compression. In Fig. 22 the comparison of the vortex core is given for several crank angles, combined with the vector field of Γ_{3p} at $Y = 0$ mm, so-called cross tumble plane, which indicates the local rotation direction.

- At -120 CAD, the vortex core appears quite similar in both cycles though the one in cycle 12 is relatively larger.

- At mid-compression, the deformation of the vortex core in cycle 10 seems to take place as the rotation direction on both sides bends up, which indicates that a tilting of the axis of rotation of the tumble structure is observed on opposite sides (near the wall). In contrast, in cycle 12 the vortex core still keeps its cylindrical form along the X axis.
- The differences are amplified during the second half of the compression. In cycle 10 the rotation direction of the lateral parts becomes much more inclined while the middle part keeps rotating around the X axis. In cycle 12, the $\|\mathbf{\Gamma}_{3p}\|$ iso-surface seems to fill the combustion chamber, which corresponds to a strong tumble motion along the X axis.
- Close to the end of the compression, the vortex core in cycle 10 breaks up into several vortices which confirms what has been first observed in Fig. 21. The rotation of the middle part remains along the X axis in cycle 10 but is much less organized than that in cycle 12.

The tumble deformation occurring in the chamber can be associated with the elliptical instability of the tumble motion as reported by Obukhov (2000) and discussed in Lumley (2001). Obukhov found that a fluid bound in a triaxial ellipsoid, initially rotating along the long axis, tends to rotate around the short axis to remain stable. Similar to in-cylinder flows, the tumble motion is initially aligned with one of the two shorter axes at BTC. During the compression, as the piston moves upward, the axis of piston movement (Z axis in this case) becomes gradually the shortest axis, which causes the tumble motion to flip and break into a pair of vortices aligned with the Z axis, as shown in Fig. 22. This type of instability has been observed in the tumble motion in (Fogleman et al 2004; Foucher et al 2008).

The local rotation intensity **RI** is then calculated for two selected engine cycles for a more quantitative comparison of the evolution of the tumble motion. The three components of **RI** represents the rotation intensity around directions X, Y, and Z and are noted classically as tumble ratio TR, cross-tumble ratio CTR, and swirl ratio SR (Jaffri et al 1997). In Fig. 23 these three components computed along the TCL in the three directions are plotted with respect to the crank angle for the two engine cycles chosen before.

The rotation intensity in the three directions provides also information about the tumble deformation. The tumble intensity along X axis TR is the main component among the three. A clear enhancement beyond -120 CAD can be seen in its evolution. In cycle 10, which experiences a significant deformation, TR between -90 and -40 CAD is larger in the lateral parts than in the middle part, which indicates a faster rotational air motion on both sides. Near the end of the compression, TR decreases to almost 0 as the local rotation is no more around the X axis. In cycle 12 during the second half of the compression, TR is more homogeneously distributed along X and conforms to the cylindrical form of the vortex core that sustains to the end of the compression.

The other two components CTR and SR offer complementary information on the tumble deformation. The deformation occurs during compression resulting in the change of the local rotation direction of the large-scale motion

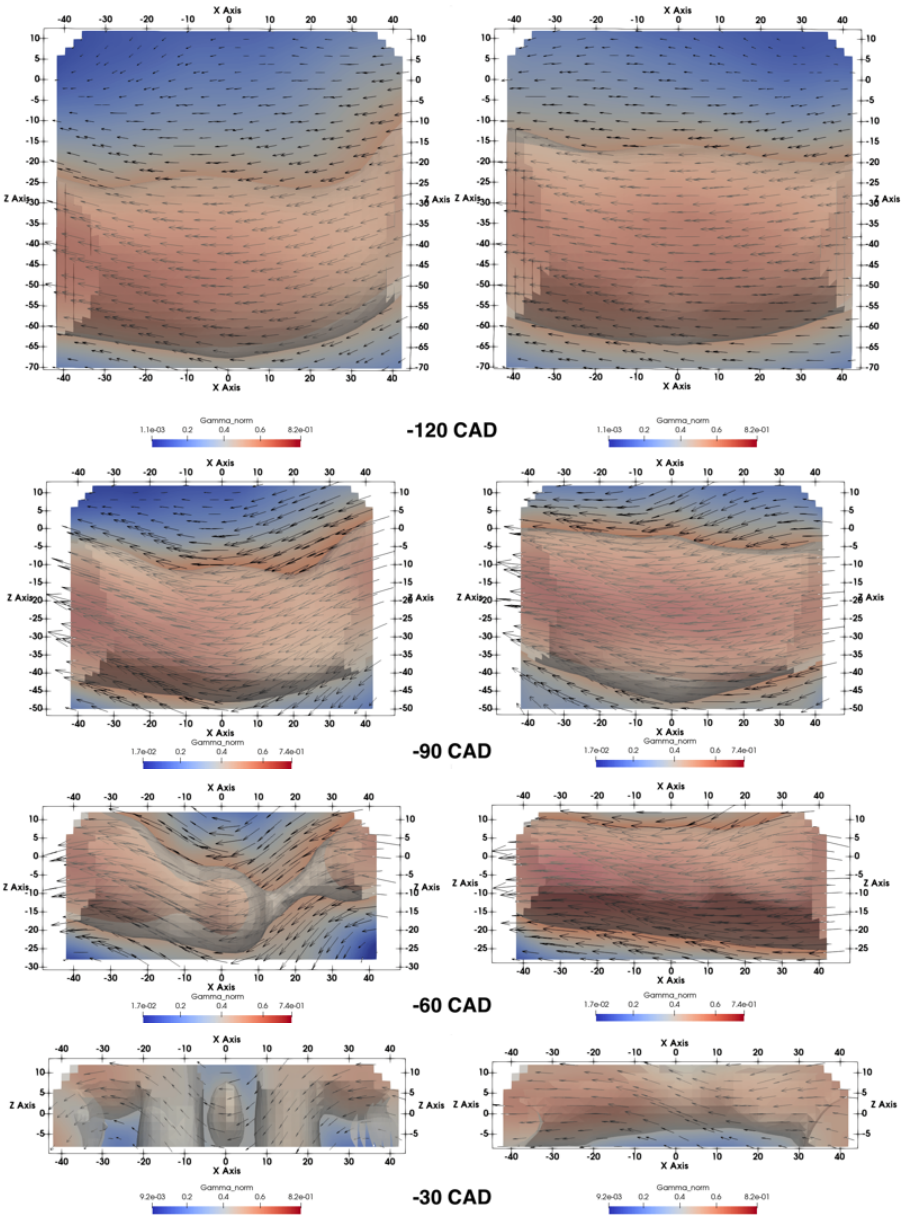

Fig. 22: Evolution of the tumble vortex core for cycles 10 (left) and 12 (right), combined with the vector field of Γ_{3p} at slice $Y = 0$ mm.

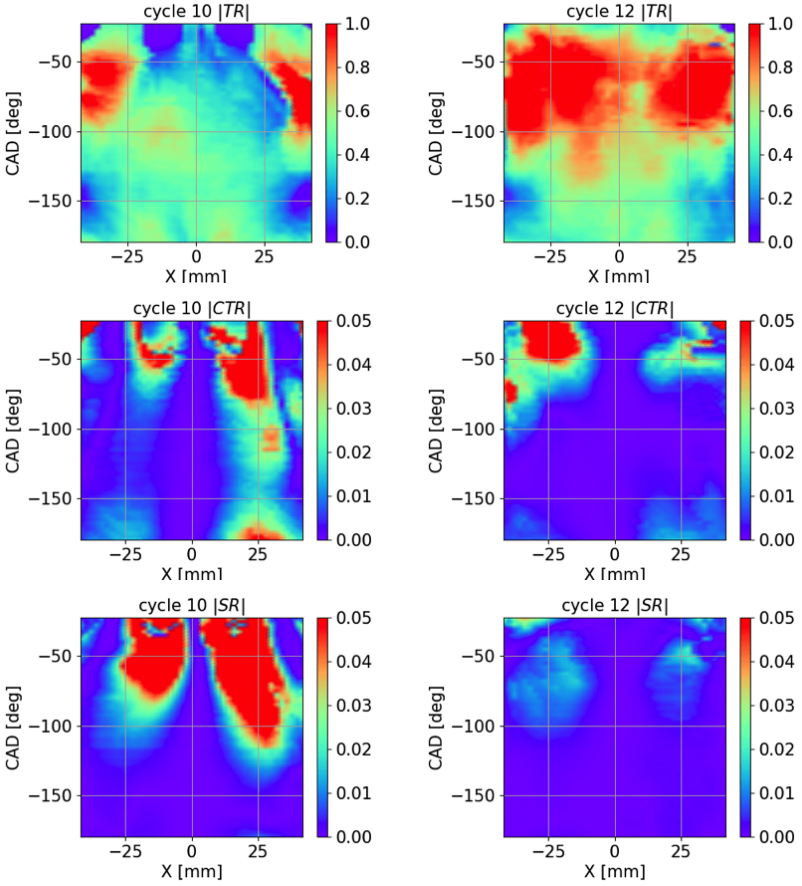

Fig. 23: Comparison of tumble intensity during compression stroke around directions X, Y, and Z for engine cycles 10 (left) and 12 (right).

which is no longer aligned with the X axis in this case. Though their values are much smaller compared to TR, the increasing of CTR and SR during compression allows us to identify the beginning of the deformation which starts at around -120 CAD in cycle 10. Noticeable differences exist already in the component CTR at the very beginning of the compression, which leads us to the hypothesis that the initial form of the tumble may be responsible for the tumble deformation.

The deformation of the tumble has been highlighted thanks to Γ_{3p} and the related angular momenta in different directions. It seems that the tumble does not completely break up into small eddies in the current engine as expected but in some particular cycles switches from a pure rotation around the X axis to a pair of counter-rotating vortices around an inclined axis in YZ plane. The large-scale motion seems to be dominant in this engine even at the end

of compression, and significant differences reside in the large-scale structures, which may explain why E_k^{CCV} contributes much more than E_k^{HF} to the kinetic energy of the fluctuating part as presented in Fig. 18b. However, it is still worth studying the energy transfer between the tumble deformation in large-scale motion and small-scale turbulence.

The turbulent part of the flow can be separated from the instantaneous velocity field with the help of 3D EMD. As we focus on the flow properties at the time corresponding to the spark-timing of the reactive case, *i.e.* −22.5 CAD, 3D EMD is applied to flow fields at this specific instant. Instead of regarding the global turbulence level, the local turbulent energy around the spark is of greater interest as it can impact the flame kernel development at the early stage of ignition which can be determinant for the whole combustion process in SI engines.

The local turbulent energy is evaluated in a sub-volume surrounding the spark plug whose size should be comparable to the turbulent integral length scale. The integral length scale can be estimated from the normalized two-point correlation function (Janas et al 2017; Sadeghi et al 2021) defined as:

$$R_{ii}(r) = \frac{\langle u_i(x_i)u(x_i + r)\rangle}{\langle u_i(x_i)^2\rangle} \tag{24}$$

In Eq. 24, the velocity u is the HF part extracted by 3D EMD, i denotes a velocity component in the direction i and $\langle\rangle$ represents the spatial average. Cycle 3 is selected for illustration, and the corresponding auto-correlation curves for each component of U_{HF} in their corresponding direction are plotted in Fig. 24.

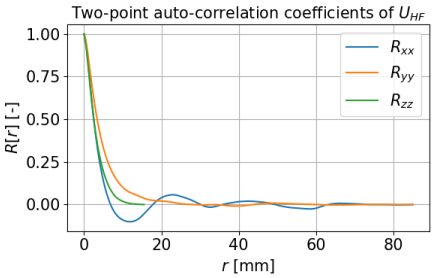

Fig. 24: Two-point auto-correlation functions of U_{HF} of cycle 3 extracted by 3D EMD, computed for each component of U_{HF} in the corresponding direction using Eq. 24.

The integral length scales in the three directions are obtained by integrating auto-correlation functions until the first zero crossing as used in Janas et al (2017) and Sadeghi et al (2021). The length scales, ensemble-averaged over the 25 cycles at ignition time, are equal to 3.1 mm, 4.6 mm and 3.3 mm respectively in X, Y and Z directions. Therefore, the sub-volume's size should be of the

order of 5 mm. A sphere of diameter 5 mm around the spark plug is chosen in this study and the averaged turbulent energy is computed (see Fig. 25a) for the following analysis.

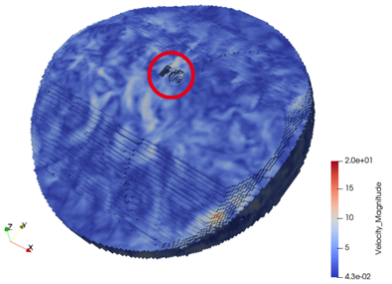

(a) HF part obtained using 3D EMD for 3D velocity field at −22.5 CAD. Evaluation of the averaged local turbulent energy E_k^{HF} (circled in red) around the spark plug.

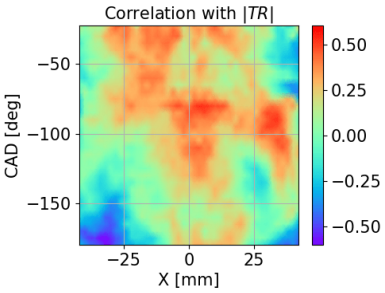

(b) Correlation map between the averaged local turbulent energy E_k^{HF} around spark plug at −22.5 CAD and the local tumble intensity $\mathrm{TR}(X, \theta)$.

Fig. 25: Relation between large-scale tumble motion and local turbulent intensity.

The component TR is representative of the tumble deformation and thus is used as a descriptor of the tumble during compression. The relation between the tumble and the resulting turbulent energy around the spark plug is investigated by computing the Pearson correlation coefficient R_{xy} between the averaged local turbulent kinetic energy at ignition $E_k^{HF}(t_{ign})$ and the tumble intensity $\mathrm{TR}(X, \theta)$ for varying crank angle θ and X coordinate. Results are plotted on a 2D map in Fig. 25b. It can be seen that regions with significant positive correlations are located in the central part of the tumble during almost the whole compression stroke. It can be inferred that a well-organized tumbling flow in the chamber that can maintain the rotational motion around the transversal axis of the cylinder and experiences slight deformation is favorable for a high level of turbulent energy around the spark which is preferred for fast combustion. A possible explanation is that a stronger tumble motion contains more kinetic energy in itself and can maintain the energy transfer to small eddies by the energy cascade, and in contrast, a weaker tumble motion, caused by the tumble deformation leads to a vortices pair near TDC, releases its energy faster to small eddies which dissipate also earlier.

4.5 The link between 2D and 3D diagnostics

The in-cylinder flow analysis was performed using both 2D and 3D analysis tools. The flow characterization in 3D did provide insight into the tumble's shape and its intensity, as well as the kinetic energy distribution in different

structure scales. Nonetheless, 3D flow can only be obtained with numerical simulations, and PIV measurements are rather available in 2D planes. In this section, we would like to explore potential links between flow characteristics obtained from 2D and 3D analysis and investigate if 2D flow features allow the prediction of 3D flow features.

In the 2D tumble central plane, the tumble motion is visible during compression, and we choose the 2D tumble ratio $|\mathrm{TR_{2D}}|$ computed from this 2D plane during the whole compression stroke from −180 to −22.5 CAD as the 2D flow features.

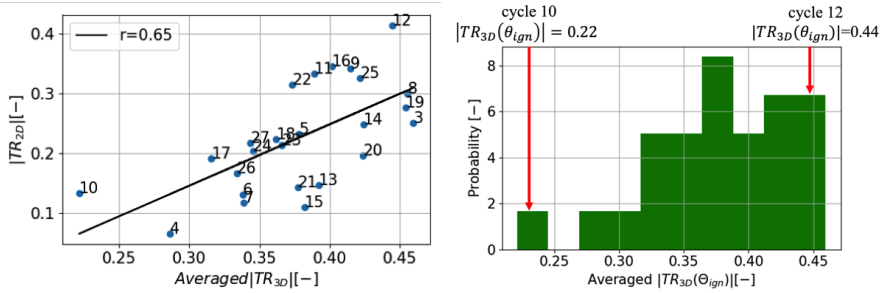

(a) Correlation between the tumble ratio of 2D and 3D at −22.5 CAD.

(b) Distribution of the 3D tumble ratio at −22.5 CAD.

Fig. 26: Relation between the tumble ratio of 2D $|\mathrm{TR_{2D}}|$ and 3D $|\mathrm{TR_{3D}}|$ at −22.5 CAD.

A scatter plot of the 2D tumble ratio $|\mathrm{TR_{2D}}|$ as a function of the averaged 3D tumble ratio $|\mathrm{TR_{3D}}|$ along the TCL at −22.5 CAD is plotted in Fig. 26a. A non-negligible correlation can be noted between these two flow features extracted from 2D and 3D flow fields, which suggests that the tumble ratio quantified in the 2D tumble central plane is a good descriptor of the flow state in 3D. The distribution of the averaged 3D tumble ratio $|\mathrm{TR_{3D}}|$ is shown in Fig. 26b. The two extreme cycles 10 and 12, which were found different in the 2D tumble central plane, behave the same way in 3D as their 3D tumble ratio are also located in the two extreme groups.

Coefficients of correlations are computed between several 3D flow features at spark timing, including the kinetic energy of the LF and HF parts extracted by 3D EMD, both in the whole chamber and the spark plug region, and 2D tumble ratio $\mathrm{TR_{2D}}(\theta)$ as a function of the crank-angle degree. Results are plotted in Fig. 27.

Significant correlations are found between $\mathrm{TR_{2D}}(\theta)$ and the global $E_k^{LF}(\theta_{ign})$ in Fig. 27a for θ close to θ_{ign}, which is normal as both of them quantify the intensity of large-scale motions. During the first half of the compression stroke, correlation coefficients between $|\mathrm{TR_{2D}}|$ and the local $E_k(\theta_{ign})$ increase for both LF (in Fig. 27c) and HF (in Fig. 27d) parts. They reach

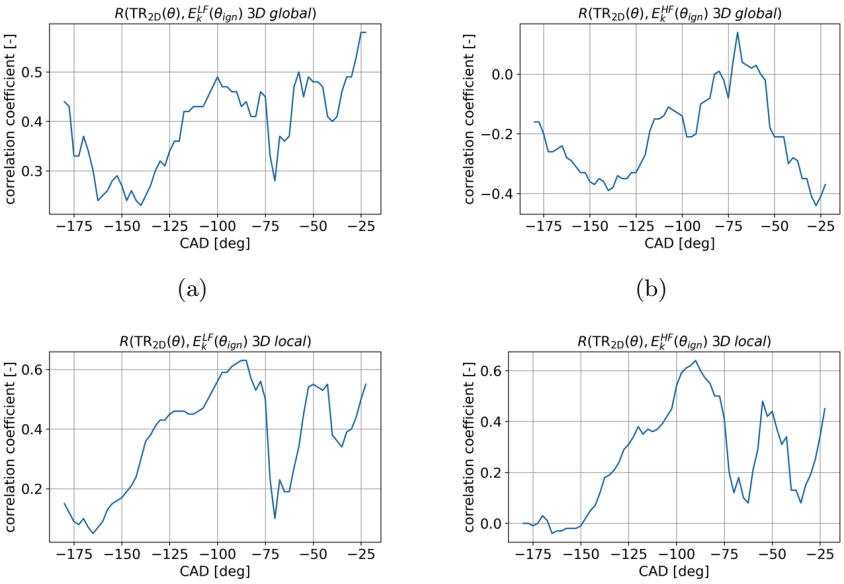

Fig. 27: Evolution of the correlation coefficient between $\mathrm{TR}_{2D}(\theta)$ and kinetic energy $E_k(\theta_{ign})$ of the LF or HF parts in the whole chamber (global) or near the spark plug (local) at $\theta_{ign} = -22.5$ CAD extracted by 3D EMD, for $-180 < \theta < 22.5$ CAD.

significant values at mid-compression, followed by a dramatic decrease after -75 CAD. According to our observation on the tumble evolution quantified by **RI** (Fig. 23), it can be noticed that some strong changes in the tumble motion occur during the second half of compression. The evolution of these two correlations could be impacted by the complex and non-linear tumble deformation, especially after -75 CAD when the tumble motion is switching to a pair of vortices for cycles of low **RI** at -22.5 CAD.

Another attempt is made to investigate the link between the LF and the HF parts of the flow, both locally and globally. The two scatter plots and corresponding coefficients of correlations plotted in Fig. 28 indicate that the global turbulence level near spark-timing does not depend on the intensity of large-scale motions. Contrarily, the local turbulent energy presents a strong dependence on the local large-scale motion, which suggests that the local turbulence is generated by the local high-velocity flow motion.

In Fig. 29 we present again the distribution of the averaged 3D tumble ratio at θ_{ign}, with each bar colored by the corresponding averaged 3D swirl ratio at θ_{ign} that quantifies the tumble deformation. A global weak tumble motion is more likely to have a high 3D swirl ratio because of the deformation, while a strong tumble motion is resistant to such a flow structure change. In future

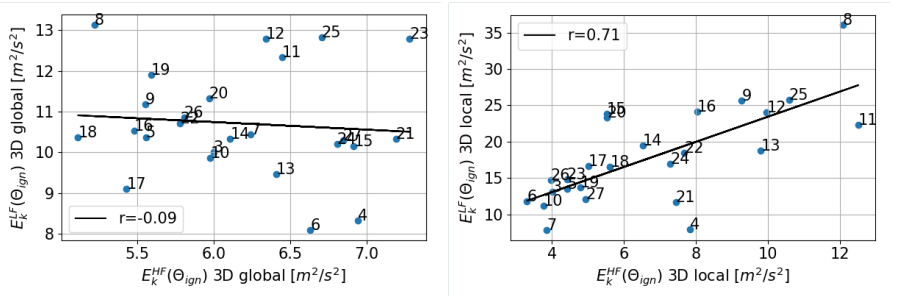

(a) (b)

Fig. 28: Correlations between kinetic energy of LF and HF parts in the whole chamber or near the spark plug at −22.5 CAD.

work, we will quantify the impact of the tumble deformation in the reactive case on the combustion process.

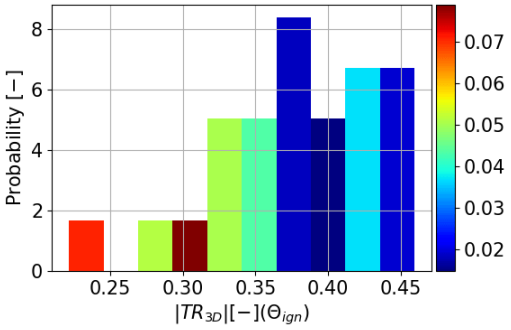

Fig. 29: Distribution of 3D tumble ratio TR at −22.5 CAD, colored by the corresponding averaged 3D swirl ratio SR in each bar.

5 Conclusions

In this work, the TU Darmstadt optical engine was simulated using LES under motored conditions for the analysis of internal aerodynamics.

An improved version of bivariate 2D EMD was proposed based on the one described in Sadeghi et al (2021). The major modification was focused on the mode combination strategy. The improved EMD got rid of the predefined number of modes and the interpolation used in Sadeghi et al (2021) to deal with time-varying geometries and was massively accelerated as the full decomposition was unnecessary. The EMD was then extended to treat trivariate 3D data

and made it possible to characterize the in-cylinder turbulence which could impact the combustion process.

In the present study, the choice of the cut-off mode between large-scale coherent structures and small-scale turbulence was based on the PSD of each velocity component and on some considerations on the characteristic scales of the flow. The separation criterion was set identically for all instants of the engine cycle, as it adapts to the varying scales of the flow. However, the question of a more universal criterion should be addressed in the future. Different methods can be found in the literature to separate the different scales, based on spatial correlations (Qin et al 2019), conditional averaging (Voisine et al 2011; Buhl et al 2016) or on the properties of turbulence (Rulli et al 2021a,b). But there are still no fully objective criteria that may affect the conclusions depending on the method used. Also, the extension of EMD in 2D and 3D was based on the principle of sequential decomposition: EMD 1D was carried out sequentially on all rows one after the other direction. Using such an approach, each line's decomposition was independent, resulting in visible discontinuities on extracted LF parts. Increasing the number of realizations NE did not fundamentally resolve the problem. Some direct extensions of EMD in 2D (Xia et al 2019) using 2D interpolation and in 3D (He et al 2017) using separable filters for envelop generation can be promising alternatives for the current EMD implementation to avoid this problem and will be explored in the future. Applying EMD at boundaries is also an issue. Several techniques were investigated to extend signals using the auto-regressive (VAR) model (Sandoval et al 2018; Zivot and Wang 2003), which were not shown in the paper for the sake of brevity. Finally, a no-extension strategy was found to perform the best and was retained in this study.

Using the described LES methodology, the prediction of thermodynamic properties matched well with the reference data provided by experiments and 0D simulation. A simplified crevice model was integrated into the LES to adjust the mass exchange between the chamber and the crevice. For the motored case, the overestimation of the in-cylinder pressure was not crucial as its impact on the prediction of internal aerodynamics was not visible (Janas et al 2017). However, a correct pressure level (and the corresponding temperature) was indeed desired for the reactive case. Once the thermodynamics was validated, the comparison with experiments continued on the prediction of aerodynamics. Using an imposed mass flow rate at inlet and no-slip conditions on valve walls with adapted mesh refinement, the predicted velocity agreed qualitatively and quantitatively well with the PIV data.

A total number of 25 LES consecutive cycles were launched for the CCV analysis of aerodynamics. For the motored case, the analysis was focused on the flow during compression. CCV in aerodynamics was first identified in the tumble plane in a 2D vision after its decomposition using 2D EMD, and it was noticed that CCV appeared to be strongly correlated with the tumble structure.

The energy transfer between different scales was also investigated. A noticeable energy transfer from the mean flow to the fluctuating part was observed beyond −70 CAD. Based on the 2D EMD analysis, it was concluded that most energy transferred from the mean flow was retained in CCV of large-scale motion while the turbulent fluctuations remained at a stable level until the end of the compression.

The analysis was extended in 3D for a more complete vision of the tumble motion. Γ_{3p} was used to describe the vortex core of the tumble at different instants during the compression. Two typical flow structures near the end of compression were found in this engine as a result of the tumble deformation: the flow could either stay rotational around the X axis or switch to a pair of counter-rotating vortices around an inclined axis in YZ plane, which supports the existence of elliptical instability in the tumbling flow as proposed by Lumley (2001). A qualitative comparison between the two engine cycles showed that differences in the vortex core existed already during the compression. The computed angular momentum in the three directions confirmed our finding with Γ_{3p}. It was observed that the flow structure at the end of compression was related to its initial form at BDC. Especially the appearance of secondary cross-tumble and swirl motions was proved to destabilize the tumble motion.

In this optical research engine, the large-scale motion was sustained until the end of compression despite the geometric changes during compression and friction with the walls. An attempt was still made to link the tumble motion and the local turbulence level around the spark. Local E_k^{HF}, extracted from 3D EMD analysis, was found positively correlated with the tumble intensity around the X axis of the central part. The local tumble intensity around the spark plug, related to the flow pattern near TDC, was thus important to generate turbulent fluctuations, suggesting a potential link between large-scale motions and small-scale turbulence.

In this work, analysis tools were applied and showed their potential for an extensive understanding of the internal aerodynamics in a SI engine under motored conditions. The analysis of the tumble motion during compression focused on two typical cycles and thus stays qualitative. Further analysis will be performed on the fired case with more LES cycles. In this work, some significant changes on the tumble during compression have been noted, and we would like to verify the existence of such a flow pattern change in the fired case and explore its potential impacts on the CCV of combustion which was not possible in the presented motored case. The origin of tumble deformation was not clear and will also be studied to seek its links with flow states of earlier stages in an engine cycle. Finally, the characterization of flow evolution during intake was not addressed in this work and will be carried out in the fired case study using analysis tools developed in this work. With the complete analysis of the in-cylinder flow during intake and compression and its impacts on the combustion process, a cause-effect chain from intake to combustion phase will be established.

Statements and Declarations

Acknowledgments. This work was granted access to the HPC resources of TGCC under allocation Number A0082B10763 from the GENCI (Grand Equipement National de Calcul Intensif) eDARI program. Marius Schmidt kindly acknowledges generous support by Deutsche Forschungsgemeinschaft through SFB/Transregio 150 Project Number 237267381-TRR150.

Conflict of Interest. The authors have no relevant financial or non-financial interests to disclose.

Ethical approval. Not applicable, because this article does not contain any studies with human or animal subjects.

Informed consent. Not applicable, because the research does not involve human participants.

Author contribution. Zhihao Ding performed simulations. Marius Schmidt organized the experimental database. Fabrice Foucher helped in the analysis of experimental results. Zhihao Ding wrote the first draft of the manuscript and all authors commented on previous versions of the manuscript. Zhihao Ding, Karine Truffin and Stéphane Jay performed the physical analysis and interpretation of the results. Jacques Borée provided help and ideas in performing analysis and interpreting the results. All authors contributed to the manuscript revision, read and approved the submitted version.

Appendix A Original bivariate 2D EMD algorithm

In Fig. A1 the bivariate 2D EMD methodology proposed in Sadeghi et al (2021) is schematically presented.

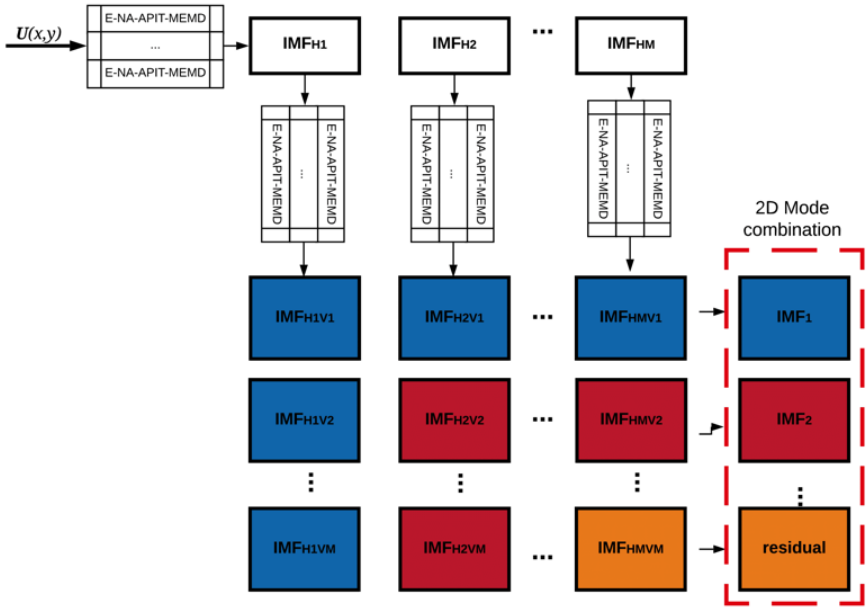

Fig. A1: Extension of EMD for 2D multivariate signals based on 1D EMD.

Appendix B Comparison of phase-averaged velocity between LES and PIV

The quantitative validation of LES results on the prediction of aerodynamics continues in this section with comparisons between LES and PIV at two instants to complete Sect. 4.

Fig. B3 compares the horizontal profiles at −180 CAD. A good agreement is found in terms of shape and amplitude, although discrepancies increase on the lower part of the tumble plane (for $Z < -24$ mm). The vertical component U_z shows larger errors than the horizontal component U_y, especially in the central part which corresponds to the central region of the tumble plane as presented in Fig. B2a. The flow predicted by LES shows a local recirculation zone on the left upper side, which generates an upward flow in the central region and thus creates a positive U_z. This observed flow structure may be attributed to a lack of convergence of the mean velocity field

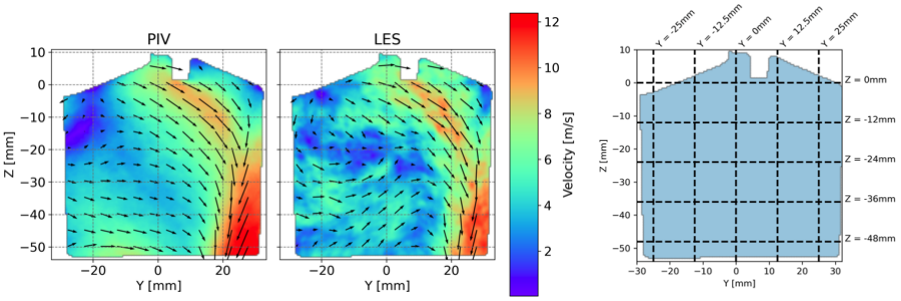

(a) (b)

Fig. B2: (a) Comparison of phase-averaged velocity between LES and PIV at −180 CAD (b) Sampling lines in the tumble plane at −180 CAD for comparison between LES results and PIV measurements.

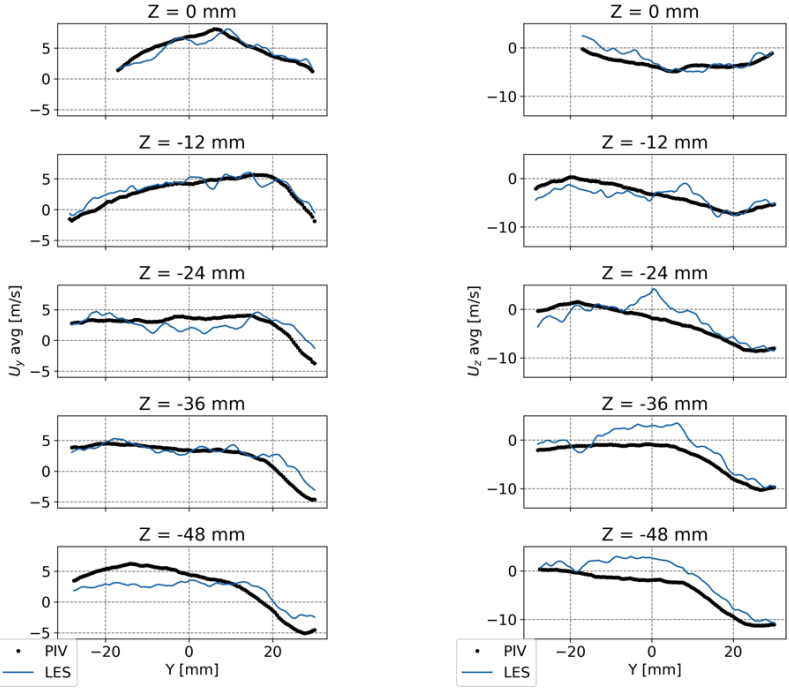

(a) U_y component (b) U_z component

Fig. B3: Comparison of 1D profiles over horizontal lines in the tumble plane at −180 CAD.

Fig. B4 illustrates the vertical profiles at −180 CAD. The same issue on the component U_z is also observed on the bottom part of vertical lines at $Y = -12.5$ mm, $Y = 0$ mm and $Y = 12.5$ mm. The component U_y agrees much better with PIV measurements except on the line at $Y = 25$ mm, which reveals the fact that the tumble flow predicted by LES is slightly weaker but remains acceptable.

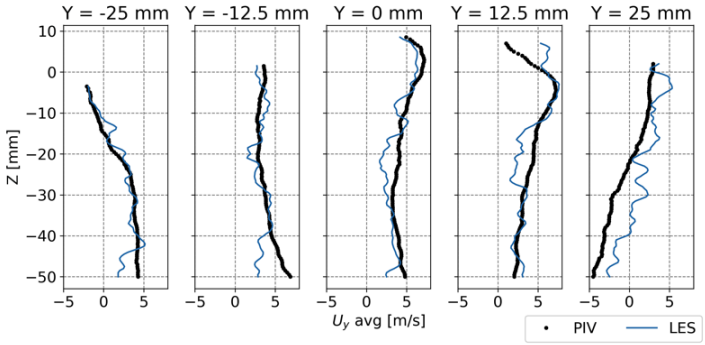

(a) U_y component.

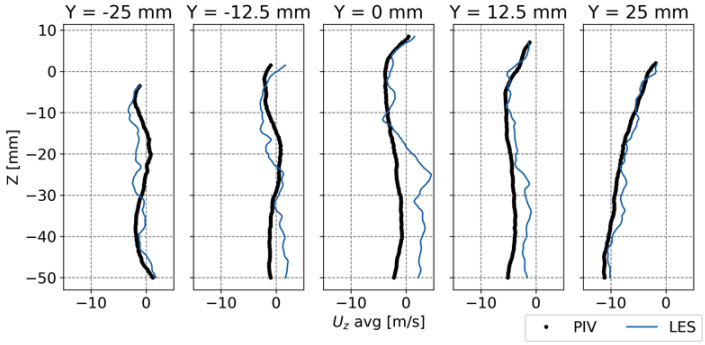

(b) U_z component.

Fig. B4: Comparison of 1D profiles over vertical lines in the tumble plane at −180 CAD.

Phase-averaged velocity fields at −270 CAD during the intake stroke obtained from LES and PIV are compared in Fig. B5a. The intake flow generated by the interaction between intake valve jets is slightly weaker as predicted by LES. The flow descends also much more deeply on the exhaust side as shown in the PIV field, contrary to the one predicted by LES that the secondary intake flow on the intake side penetrates more in the chamber.

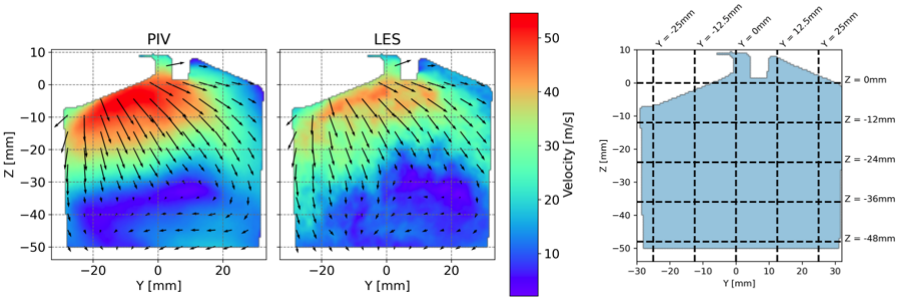

(a) (b)

Fig. B5: (a) Comparison of phase-averaged velocity between LES and PIV at −270 CAD (b) Sampling lines in the tumble plane at −270 CAD for comparison between LES results and PIV measurements.

The comparison of velocity profiles on horizontal sampling lines indicated in Fig. B5b is illustrated in Fig. B6. On the component U_y, LES results match well PIV data except on the line $Z = -48$ mm near the piston where U_y is globally smaller cause LES does not capture the arrival of primary intake flow as shown in Fig. B5a. Concerning the component U_z, differences can be observed on the line $Z = -12$ mm laying inside the interaction zone and also on the lateral sides of the line $Z = -36$ mm where primary and secondary intake jets pass through.

Velocity profiles on vertical sampling lines are compared in Fig. B7 between LES and PIV. Similar to the comparison on horizontal lines, most disparity exists in the region of interaction and on both the intake and exhaust sides where primary and secondary intake flows descend.

The phase-average velocity fields at −90 CAD during compression stroke obtained from LES and PIV are compared in Fig. B8a. The flow pattern is of a classical tumble motion which is moving upward. LES tends to predict a weaker tumble motion than what has been captured by PIV.

The comparison is also made on horizontal and vertical sampling lines plotted in Fig. B8b. For both horizontal and vertical lines, discrepancies are all located in the region around the tumble front, otherwise, a general accord exists between LES and PIV.

Considering that the phase-averaged velocity field is not statistically fully converged, only a qualitative comparison of the simulated and measured root

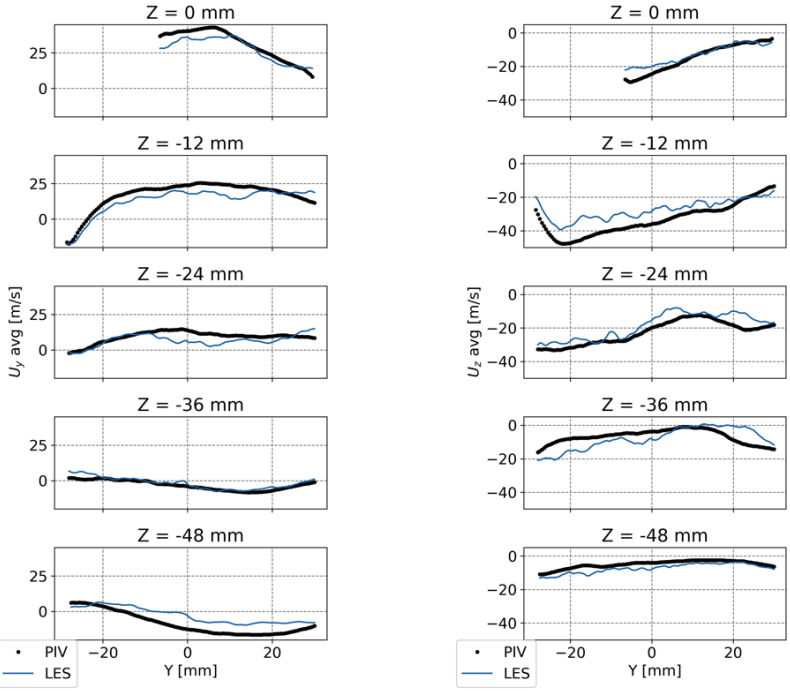

(a) U_y component. (b) U_z component.

Fig. B6: Comparison of 1D profiles over horizontal lines in the tumble plane at −270 CAD.

mean square (RMS) velocity is presented hereafter in Fig. B11. It can be seen that regions of significant fluctuations are well captured by LES for both the right side, where the tumble flow is descending, and the left side, where the tumble front begins to move upwards.

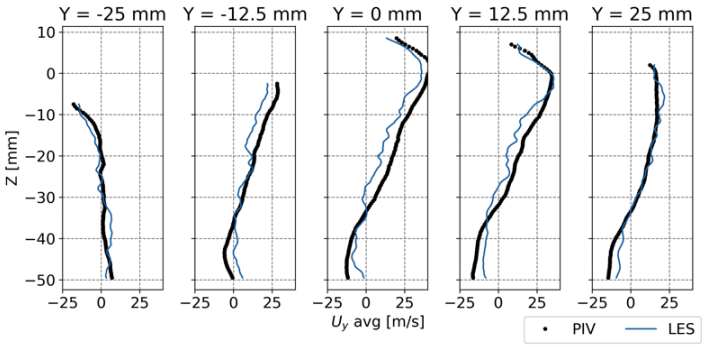

(a) U_y component.

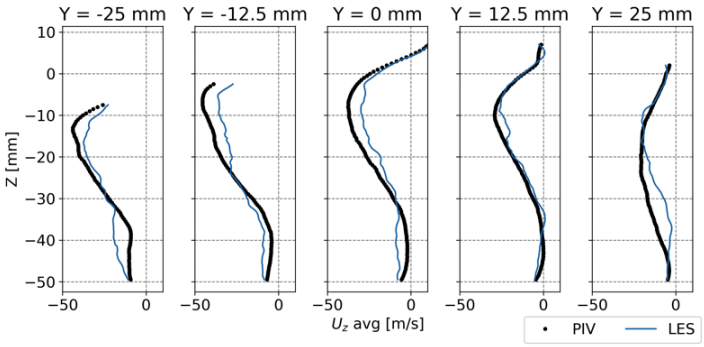

(b) U_z component.

Fig. B7: Comparison of 1D profiles over vertical lines in the tumble plane at −270 CAD.

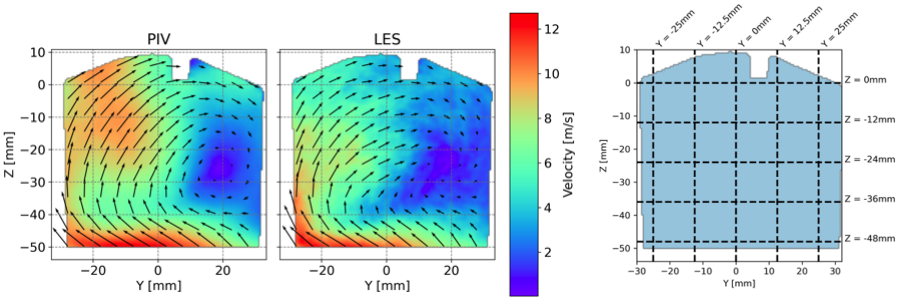

(a) (b)

Fig. B8: (a) Comparison of phase-averaged velocity between LES and PIV at −90 CAD (b) Sampling lines in the tumble plane at −90 CAD for comparison between LES results and PIV measurements.

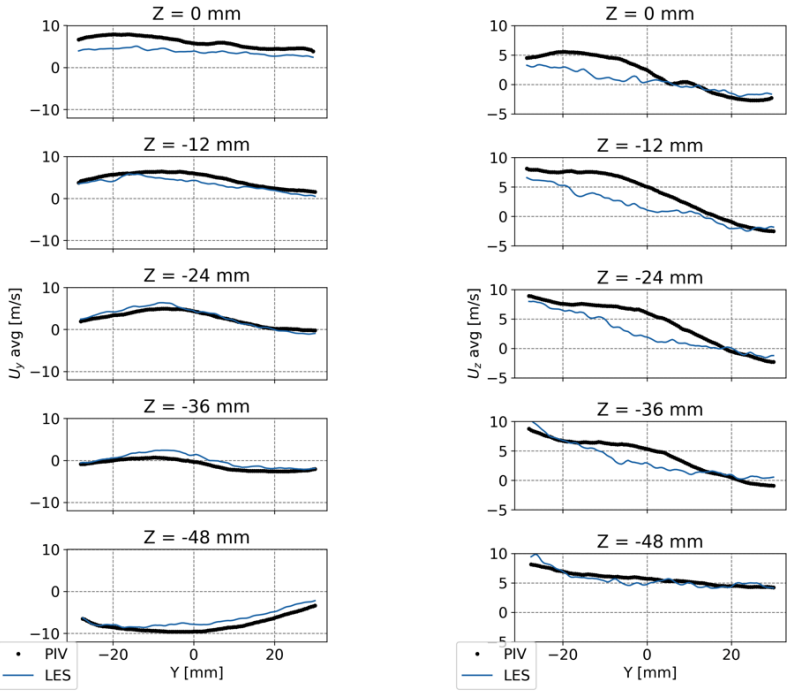

(a) U_y component. (b) U_z component.

Fig. B9: Comparison of 1D profiles over horizontal lines in the tumble plane at −90 CAD.

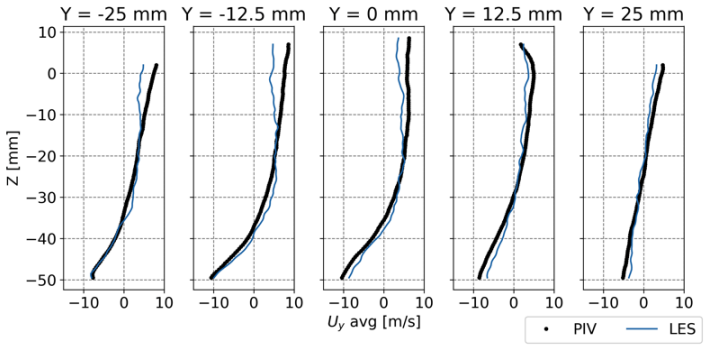

(a) U_y component.

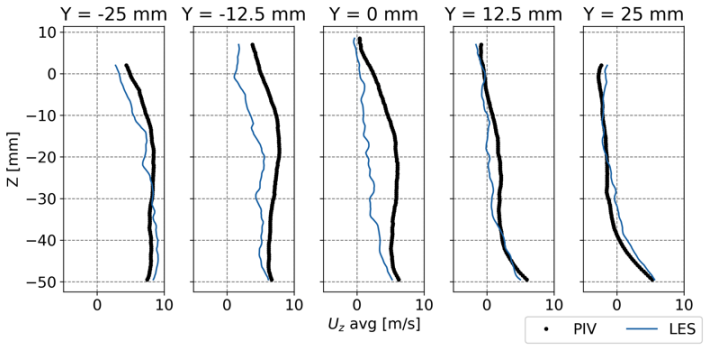

(b) U_z component.

Fig. B10: Comparison of 1D profiles over vertical lines in the tumble plane at −90 CAD.

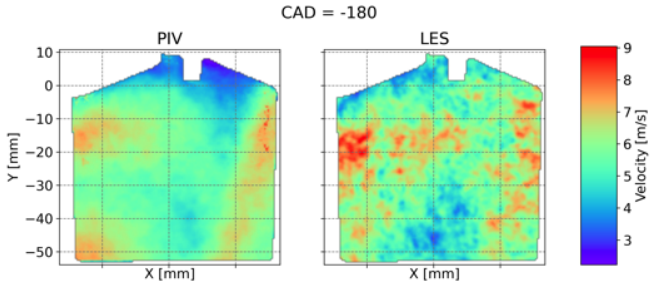

Fig. B11: Comparison of the RMS velocity in the tumble plane at −180 CAD.

References

Agostini, L., Leschziner, M.: On the influence of outer large-scale structures on near-wall turbulence in channel flow. Phys. Fluids **26**(7), 075107 (2014) https://doi.org/10.1063/1.4890745

Agostini, L., Leschziner, M.: Predicting the response of small-scale near-wall turbulence to large-scale outer motions. Phys. Fluids **28**(1), 015107 (2016) https://doi.org/10.1063/1.4939712

Agostini, L., Leschziner, M.: The impact of footprints of large-scale outer structures on the near-wall layer in the presence of drag-reducing spanwise wall motion. Flow, Turbul. Combust. **100**(4), 1037–1061 (2018) https://doi.org/10.1007/s10494-018-9917-3

Agostini, L., Leschziner, M.: The connection between the spectrum of turbulent scales and the skin-friction statistics in channel flow at $Re_\tau \approx 1000$. J. Fluid Mech. **871**, 22–51 (2019) https://doi.org/10.1017/jfm.2019.297

Agostini, L., Leschziner, M.: Auto-encoder-assisted analysis of amplitude and wavelength modulation of near-wall turbulence by outer large-scale structures in channel flow at friction reynolds number of 5200. Phys. Fluids **34**(11), 115142 (2022) https://doi.org/10.1063/5.0123119

Altaf, M. U. B., Gautama, T., Tanaka, T., Mandic, D. P.: Rotation invariant complex empirical mode decomposition. In: 2007 IEEE International Conference on Acoustics, Speech and Signal Processing - ICASSP '07, III-1009-III-1012 (2007) https://doi.org/10.1109/ICASSP.2007.366853

Amsden, A.: KIVA-3V: A block-structured KIVA program for engines with vertical or canted valves. Tech. rep., Los Alamos National Laboratory (LANL) (1997) https://doi.org/10.2172/505339

Anindya, C.: An introduction to the proper orthogonal decomposition. Curr. Sci. **78**(7), 808–817 (2000)

Baum, E., Peterson, B., Böhm, B., Dreizler, A.: On the validation of LES applied to internal combustion engine flows: Part I: Comprehensive experimental database. Flow, Turbul. Combust. **92**(1-2), 269–297 (2014) https://doi.org/10.1007/s10494-013-9468-6

Baumann, M., Di Mare, F., Janicka, J.: On the validation of large eddy simulation applied to internal combustion engine flows part II: Numerical analysis. Flow, Turbul. Combust. **92**(1-2), 299–317 (2014) https://doi.org/10.1007/s10494-013-9472-x

Bode, J., Schorr, J., Krüger, C., Dreizler, A., Böhm, B.: Influence of the in-cylinder flow on cycle-to-cycle variations in lean combustion DISI engines measured by high-speed scanning-piv. Proc. Combust. Inst. **37**(4), 4929–4936 (2019) https://doi.org/10.1016/j.proci.2018.07.021

Borée, J., Miles, P. C.: In-Cylinder Flow. In: Encyclopedia of Automotive Engineering, John Wiley & Sons, Ltd, 1–31 (2014) https://doi.org/10.1002/9781118354179.auto119

Bücker, I., Karhoff, D.-C., Klaas, M., Schröder, W.: Stereoscopic multi-planar PIV measurements of in-cylinder tumbling flow. Exp. Fluids **53**(6), 1993–2009 (2012) https://doi.org/10.1007/s00348-012-1402-5

Buhl, S., Hartmann, F., Hasse, C.: Identification of large-scale structure fluctuations in IC engines using POD-based conditional averaging. Oil Gas Sci. Technol. **71**(1), 1 (2016) https://doi.org/10.2516/ogst/2015021

Buhl, S., Gleiss, F., Köhler, M., Hartmann, F., Messig, D., Brücker, C., Hasse, C.: A combined numerical and experimental study of the 3D tumble structure and piston boundary layer development during the intake stroke of a gasoline engine. Flow, Turbul. Combust. **98**(2), 579–600 (2017a) https://doi.org/10.1007/s10494-016-9754-1

Buhl, S., Hartmann, F., Kaiser, S. A., Hasse, C.: Investigation of an IC engine intake flow based on highly resolved LES and PIV. Oil Gas Sci. Technol. **72**(3), 15 (2017b) https://doi.org/10.2516/ogst/2017012

Buhl, S., Hain, D., Hartmann, F., Hasse, C.: A comparative study of intake and exhaust port modeling strategies for scale-resolving engine simulations. Int. J. Engine Res. **19**(3), 282–292 (2018) https://doi.org/10.1177/1468087417707452

Chen, H., Reuss, D. L., Sick, V.: On the use and interpretation of proper orthogonal decomposition of in-cylinder engine flows. Meas. Sci. Technol. **23**(8), 085302 (2012) https://doi.org/10.1088/0957-0233/23/8/085302

Ding, Z., Truffin, K., Jay, S., Sinoquet, D.: Uncertainty and sensitivity analysis in turbulent pipe flow simulation. In: 14th WCCM-ECCOMAS Congress 2020 (2021) https://doi.org/10.23967/wccm-eccomas.2020.185

Enaux, B., Granet, V., Vermorel, O., Lacour, C., Pera, C., Angelberger, C., Poinsot, T.: LES study of cycle-to-cycle variations in a spark ignition engine. Proc. Combust. Inst. **33**(2), 3115–3122 (2011) https://doi.org/10.1016/j.proci.2010.07.038

Fogleman, M., Lumley, J., Rempfer, D., Haworth, D.: Application of the proper orthogonal decomposition to datasets of internal combustion engine flows.

J. Turbul. **5**, N23 (2004) https://doi.org/10.1088/1468-5248/5/1/023

Fontanesi, S., d'Adamo, A., Rutland, C. J.: Large-eddy simulation analysis of spark configuration effect on cycle-to-cycle variability of combustion and knock. Int. J. Engine Res. **16**(3), 403–418 (2015) https://doi.org/10.1177/1468087414566253

Foucher, F., Landry, L., Halter, F., Mounaïm-Rousselle, C.: Turbulent flow fields analysis of a spark-ignition engine as function of the boosted pressure. In: 14th International Symposium on Laser Techniques to Fluid Mechanics, Lisboa, Portugal (2008) https://hal-univ-orleans.archives-ouvertes.fr/hal-01276316

Freudenhammer, D., Peterson, B., Ding, C.-P., Boehm, B., Grundmann, S.: The influence of cylinder head geometry variations on the volumetric intake flow captured by magnetic resonance velocimetry. SAE Tech. Pap. 2015-01-1697 (2015) https://doi.org/10.4271/2015-01-1697

Funk, C., Sick, V., Reuss, D. L., Dahm, W. J. A.: Turbulence properties of high and low swirl in-cylinder flows. SAE Tech. Pap. 2002-01-2841 (2002) https://doi.org/10.4271/2002-01-2841

Gao, Y., Ge, G., Sheng, Z., Sang, E.: Analysis and solution to the mode mixing phenomenon in EMD. In: 2008 Congress on Image and Signal Processing, 223–227 (2008) https://doi.org/10.1109/CISP.2008.193

Ghaderi Masouleh, M., Keskinen, K., Kaario, O., Kahila, H., Wright, Y. M., Vuorinen, V.: Flow and thermal field effects on cycle-to-cycle variation of combustion: scale-resolving simulation in a spark ignited simplified engine configuration. Appl. Energy **230**, 486–505 (2018) https://doi.org/10.1016/j.apenergy.2018.08.046

Gohlke, M., Beaudoin, J. F., Amielh, M., Anselmet, F.: Thorough analysis of vortical structures in the flow around a yawed bluff body. J. Turbul. **9**, N15 (2008) https://doi.org/10.1080/14685240802010657

Goryntsev, D., Sadiki, A., Klein, M., Janicka, J.: Large eddy simulation based analysis of the effects of cycle-to-cycle variations on air-fuel mixing in realistic DISI IC-engines. Proc. Combust. Inst. **32**(2), 2759–2766 (2009) https://doi.org/10.1016/j.proci.2008.06.185

Graftieaux, L., Michard, M., Grosjean, N.: Combining PIV, POD and vortex identification algorithms for the study of unsteady turbulent swirling flows. Meas. Sci. Technol. **12**(9), 1422–1429 (2001) https://doi.org/10.1088/0957-0233/12/9/307

Granet, V., Vermorel, O., Lacour, C., Enaux, B., Dugué, V., Poinsot, T.: Large-eddy simulation and experimental study of cycle-to-cycle variations of stable and unstable operating points in a spark ignition engine. Combust. Flame. **159**(4), 1562–1575 (2012) https://doi.org/10.1016/j.combustflame.2011.11.018

Hanuschkin, A., Schober, S., Bode, J., Schorr, J., Böhm, B., Krüger, C., Peters, S.: Machine learning–based analysis of in-cylinder flow fields to predict combustion engine performance. Int. J. Engine Res. **22**(1), 257–272 (2021) https://doi.org/10.1177/1468087419833269

Haussmann, M., Ries, F., Jeppener-Haltenhoff, J. B., Li, Y., Schmidt, M., Welch, C., Illmann, L., Böhm, B., Nirschl, H., Krause, M. J., Sadiki, A.: Evaluation of a near-wall-modeled large eddy lattice boltzmann method for the analysis of complex flows relevant to IC engines. Comput. **8**(2), 43 (2020) https://doi.org/10.3390/computation8020043

Haworth, D. C.: Large-eddy simulation of in-cylinder flows. Oil Gas Sci. Technol. **54**(2), 175–185 (1999) https://doi.org/10.2516/ogst:1999012

He, Z., Li, J., Liu, L., Shen, Y.: Three-dimensional empirical mode decomposition (TEMD): A fast approach motivated by separable filters. Signal Process. **131**, 307–319 (2017) https://doi.org/https://doi.org/10.1016/j.sigpro.2016.08.024

Hemakom, A., Goverdovsky, V., Looney, D., Mandic, D. P.: Adaptive-projection intrinsically transformed multivariate empirical mode decomposition in cooperative brain-computer interface applications. Phil. Trans. R. Soc. A. **374**(2065), 20150199 (2016) https://doi.org/10.1098/rsta.2015.0199

Heywood, J. B., Internal combustion engine fundamentals, 2nd edn. McGraw-Hill Education, New York (2018)

Huang, N. E., Shen, Z., Long, S. R., Wu, M. C., Shih, H. H., Zheng, Q., Yen, N.-C., Tung, C. C., Liu, H. H.: The empirical mode decomposition and the hilbert spectrum for nonlinear and non-stationary time series analysis. Proc. Math. Phys. Eng. **454**(1971), 903–995 (1998) https://doi.org/10.1098/rspa.1998.0193

Huang, N. E., Shen, Z., Long, S. R.: A new view of nonlinear water waves: The Hilbert spectrum. Annu. Rev. Fluid Mech. **31**(1), 417–457 (1999) https://doi.org/10.1146/annurev.fluid.31.1.417

Iacovano, C., Berni, F., Barbato, A., Fontanesi, S.: A preliminary 1D-3D analysis of the Darmstadt research engine under motored condition. E3S Web of Conferences **197**, 06006 (2020) https://doi.org/10.1051/e3sconf/202019706006

Iacovano, C., d'Adamo, A., Fontanesi, S., Ilio, G. D., Krastev, V. K.: A wall-adapted zonal URANS/LES methodology for the scale-resolving simulation of engine flows. Int. J. Engine Res. **23**(10), 1732–1747 (2022) https://doi.org/10.1177/14680874211032379

Impagnatiello, M., Bolla, M., Keskinen, K., Giannakopoulos, G., Frouzakis, C. E., Wright, Y. M., Boulouchos, K.: Systematic assessment of data-driven approaches for wall heat transfer modelling for LES in IC engines using DNS data. Int. J. Heat Mass Transf. **183**, 122109 (2022) https://doi.org/10.1016/j.ijheatmasstransfer.2021.122109

Issa, R.: Solution of the implicitly discretised fluid flow equations by operator-splitting. J. Comp. Phys. **62**(1), 40–65 (1986) https://doi.org/10.1016/0021-9991(86)90099-9

Jaffri, K., Hascher, H. G., Novak, M., Lee, K., Schock, H., Bonne, M., Keller, P.: Tumble and swirl quantification within a motored four-valve SI engine cylinder based on 3-D LDV measurements. SAE Tech. Pap. 970792 (1997) https://doi.org/10.4271/970792

Janas, P., Wlokas, I., Böhm, B., Kempf, A.: On the evolution of the flow field in a spark ignition engine. Flow, Turbul. Combust. **98**(1), 237–264 (2017) https://doi.org/10.1007/s10494-016-9744-3

Joo, S. H., Srinivasan, K. K., Lee, K. C., Bell, S. R.: The behaviourt of small- and large-scale variations of in-cylinder flow during intake and compression strokes in a motored four-valve spark ignition engine. Int. J. Engine Res. **5**(4), 317–328 (2004) https://doi.org/10.1243/146808704323224222

Karypis, G., Schloegel, K., Kumar, V.: PARMETIS: Parallel graph partitioning and sparse matrix ordering library. Tech. rep., University of Minnesota (1997) https://conservancy.umn.edu/handle/11299/215345

Koch, J., Schmitt, M., Wright, Y. M., Steurs, K., Boulouchos, K.: Les multi-cycle analysis of the combustion process in a small SI engine. SAE Tech. Pap. 2014-01-1138 (2014) https://doi.org/10.4271/2014-01-1138

Krüger, C., Schorr, J., Nicollet, F., Bode, J., Dreizler, A., Böhm, B.: Cause-and-effect chain from flow and spray to heat release during lean gasoline combustion operation using conditional statistics. Int. J. Engine Res. **18**(1-2), 143–154 (2017) https://doi.org/10.1177/1468087416686721

Liu, K., Haworth, D. C.: Development and assessment of POD for analysis of turbulent flow in piston engines. SAE Tech. Pap. 2011-01-0830 (2011) https://doi.org/10.4271/2011-01-0830

Liu, K., Haworth, D. C., Yang, X., Gopalakrishnan, V.: Large-eddy simulation of motored flow in a two-valve piston engine: POD analysis and cycle-to-cycle variations. Flow, Turbul. Combust. **91**(2), 373–403 (2013) https://doi.org/10.1007/s10494-013-9475-7

Lumley, J. L.: The structure of inhomogeneous turbulent flows. In: Atmospheric Turbulence and Radio Wave Propagation, Nauka, 166–178 (1967)

Lumley, J. L.: Earlt work on fluid mechanics in the IC engine. Annu. Rev. Fluid Mech. **33**(1), 319–338 (2001) https://doi.org/10.1146/annurev.fluid.33.1.319

Mandanis, C., Schmitt, M., Koch, J., Wright, Y. M., Boulouchos, K.: Wall heat flux and thermal stratification investigations during the compression stroke of an engine-like geometry: A comparison between LES and DNS. Flow, Turbul. Combust. **100**(3), 769–795 (2018) https://doi.org/10.1007/s10494-017-9879-x

Matsuda, M., Yokomori, T., Iida, N.: Investigation of cycle-to-cycle variation of turbulent flow in a high-tumble SI engine. SAE Tech. Pap. 2017-01-2210 (2017) https://doi.org/10.4271/2017-01-2210

Naitoh, K., Itoh, T., Takagi, Y., Kuwahara, K.: Large eddy simulation of premixed-flame in engine based on the multi-level formulation and the renormalization group theory. SAE Tech. Pap. 920590 (1992) https://doi.org/10.4271/920590

Nguyen, T. M., Proch, F., Wlokas, I., Kempf, A. M.: Large eddy simulation of an internal combustion engine using an efficient immersed boundary technique. Flow, Turbul. Combust. **97**(1), 191–230 (2016) https://doi.org/10.1007/s10494-015-9683-4

Nicollet, F., Analysis of cyclic phenomena in a gasoline direct injection engine of flow and mixture formation using large-eddy simulation and high-speed particle image velocimetry. PhD thesis, Technische Universität (2019) http://tuprints.ulb.tu-darmstadt.de/8385/

Nicollet, F., Krüger, C., Schorr, J., Nicoud, E., Colin, O., Angelberger, C., Bode, J., Böhm, B.: A PIV-guided large-eddy simulation of in-cylinder flows. Oil Gas Sci. Technol. **72**(5), 28 (2017) https://doi.org/10.2516/ogst/2017022

Nicoud, F., Toda, H. B., Cabrit, O., Bose, S., Lee, J.: Using singular values to build a subgrid-scale model for large eddy simulations. Phys. Fluids **23**(8), 085106 (2011) https://doi.org/10.1063/1.3623274

Obukhov, A. M.: Turbulence and atmospheric dynamics, english translation edited by J. L. Lumley. CTR Monograph **2**, 1429–1439 (2000)

Ozdor, N., Dulger, M., Sher, E.: Cyclic variability in spark ignition engines a literature survey. SAE Tech. Pap. 940987 (1994) https://doi.org/10.4271/940987

Qin, W., Xie, M., Jia, M., Wang, T., Liu, D.: Large eddy simulation and proper orthogonal decomposition analysis of turbulent flows in a direct injection spark ignition engine: Cyclic variation and effect of valve lift. Sci. China Technol. Sci. **57**(3), 489–504 (2014) https://doi.org/10.1007/s11431-014-5472-x

Qin, W., Zhou, L., Liu, D., Jia, M., Xie, M.: Investigation of in-cylinder engine flow quadruple decomposition dynamical behavior using proper orthogonal decomposition and dynamic mode decomposition methods. J. Eng. Gas Turbines Power **141** (2019) https://doi.org/10.1115/1.4042725/374477

Richards, K. J., Senecal, P. K., Pomraning, E., Converge 2.4.6 Theory Manual. Convergent Science, Madison, WI (2017)

Richards, K. J., Senecal, P. K., Pomraning, E., Converge 3.0. Convergent Science, Madison, WI (2022)

Rilling, G., Flandrin, P., Goncalves, P., Lilly, J. M.: Bivariate empirical mode decomposition. IEEE Signal Processing Letters **14**(12), 936–939 (2007) https://doi.org/10.1109/LSP.2007.904710

Roudnitzky, S., Druault, P., Guibert, P.: Proper orthogonal decomposition of in-cylinder engine flow into mean component, coherent structures and random gaussian fluctuations. J. Turbul. **7**, N70 (2006) https://doi.org/10.1080/14685240600806264

Rulli, F., Barbato, A., Fontanesi, S., d'Adamo, A.: Large eddy simulation analysis of the turbulent flow in an optically accessible internal combustion engine using the overset mesh technique. Int. J. Engine Res. **22**(5), 1440–1456 (2021a) https://doi.org/10.1177/1468087419896469

Rulli, F., Fontanesi, S., d'Adamo, A., Berni, F.: A critical review of flow field analysis methods involving proper orthogonal decomposition and quadruple proper orthogonal decomposition for internal combustion engines. Int. J. Engine Res. **22**(1), 222–242 (2021b) https://doi.org/10.1177/1468087419836178

Sadeghi, M., Foucher, F., Abed-Meraim, K., Mounaïm-Rousselle, C.: Bivariate 2D empirical mode decomposition for analyzing instantaneous turbulent velocity field in unsteady flows. Exp. Fluids **60**(8) (2019) https://doi.org/10.1007/s00348-019-2775-5

Sadeghi, M., Truffin, K., Peterson, B., Böhm, B., Jay, S.: Development and application of bivariate 2D-EMD for the analysis of instantaneous flow structures and cycle-to-cycle variations of in-cylinder flow. Flow, Turbul. Combust. **106**(1), 231–259 (2021) https://doi.org/10.1007/s10494-020-00197-z

Sandoval, S., Bredin, M., De Leon, P. L.: Using linear prediction to mitigate end effects in empirical mode decomposition. In: 2018 IEEE Global Conference on Signal and Information Processing (GlobalSIP), 281–285 (2018) https://doi.org/10.1109/GlobalSIP.2018.8646563

Schmidt, M., Ding, C.-P., Peterson, B., Dreizler, A., Böhm, B.: Near-wall flame and flow measurements in an optically accessible SI engine. Flow, Turbul. Combust. **106**(2), 597–611 (2021) https://doi.org/10.1007/s10494-020-00147-9

Schmitt, M., Frouzakis, C. E., Tomboulides, A. G., Wright, Y. M., Boulouchos, K.: Direct numerical simulation of the effect of compression on the flow, temperature and composition under engine-like conditions. Proc. Combust. Inst. **35**(3), 3069–3077 (2015) https://doi.org/10.1016/j.proci.2014.06.097

Sirovich, L.: Turbulence and the dynamics of coherent structures. I. coherent structures. Q. Appl. Math. **45**(3), 561–571 (1987a) https://doi.org/10.1090/qam/910462

Sirovich, L.: Turbulence and the dynamics of coherent structures. II. symmetries and transformations. Q. Appl. Math. **45**(3), 573–582 (1987b) https://doi.org/10.1090/qam/910463

Sirovich, L.: Turbulence and the dynamics of coherent structures. III. dynamics and scaling. Q. Appl. Math. **45**(3), 583–590 (1987c) https://doi.org/10.1090/qam/910464

Sjerić, M., Kozarac, D., Tatschl, R.: Modelling of early flame kernel growth towards a better understanding of cyclic combustion variability in SI engines. Energy Convers. Manag. **103**, 895–909 (2015) https://doi.org/10.1016/j.enconman.2015.07.031

Stiehl, R., Bode, J., Schorr, J., Krüger, C., Dreizler, A., Böhm, B.: Influence of intake geometry variations on in-cylinder flow and flow–spray interactions in a stratified direct-injection spark-ignition engine captured by time-resolved particle image velocimetry. Int. J. Engine Res. **17**(9), 983–997 (2016) https://doi.org/10.1177/1468087416633541

Tanaka, T., Mandic, D. P.: Complex empirical mode decomposition. IEEE Signal Process. Lett. **14**(2), 101–104 (2007) https://doi.org/10.1109/LSP.2006.882107

Thobois, L., Lauvergne, R., Poinsot, T.: Using LES to investigate reacting flow physics in engine design process. SAE Tech. Pap. 2007-01-0166 (2007) https://doi.org/10.4271/2007-01-0166

Toledo, M. S., Le Penven, L., Buffat, M., Cadiou, A., Padilla, J.: Large eddy simulation of the generation and breakdown of a tumbling flow. Int. J. Heat Fluid Flow **28**(1), 113–126 (2007) https://doi.org/10.1016/j.ijheatfluidflow.2006.03.029

Truffin, K., Angelberger, C., Richard, S., Pera, C.: Using large-eddy simulation and multivariate analysis to understand the sources of combustion cyclic variability in a spark-ignition engine. Combust. Flame. **162**(12), 4371–4390 (2015) https://doi.org/10.1016/j.combustflame.2015.07.003

ur Rehman, N., Mandic, D. P.: Empirical mode decomposition for trivariate signals. IEEE Trans. Signal Process. **58**(3), 1059–1068 (2010) https://doi.org/10.1109/TSP.2009.2033730

ur Rehman, N., Mandic, D. P.: Filter bank property of multivariate empirical mode decomposition. IEEE Trans. Signal Process. **59**(5), 2421–2426 (2011) https://doi.org/10.1109/TSP.2011.2106779

ur Rehman, N., Park, C., Huang, N. E., Mandic, D. P.: EMD via MEMD: Multivariate noise-aided computation of standard EMD. Adv. Adapt. Data Anal. **05**(02), 1350007 (2013) https://doi.org/10.1142/S1793536913500076

Vermorel, O., Richard, S., Colin, O., Angelberger, C., Benkenida, A., Veynante, D.: Multi-cycle LES simulations of flow and combustion in a PFI SI 4-valve production engine. SAE Tech. Pap. 2007-01-0151 (2007) https://doi.org/10.4271/2007-01-0151

Voisine, M., Thomas, L., Borée, J., Rey, P.: Spatio-temporal structure and cycle to cycle variations of an in-cylinder tumbling flow. Exp. Fluids **50**(5), 1393–1407 (2011) https://doi.org/10.1007/s00348-010-0997-7

Wadekar, S., Janas, P., Oevermann, M.: Large-eddy simulation study of combustion cyclic variation in a lean-burn spark ignition engine. Appl. Energy **255**, 113812 (2019) https://doi.org/10.1016/j.apenergy.2019.113812

Welch, C., Schmidt, M., Keskinen, K., Giannakopoulos, G., Boulouchos, K., Dreizler, A., Boehm, B.: The effects of intake pressure on in-cylinder gas velocities in an optically accessible single-cylinder research engine. SAE Tech. Pap. 2020-01-0792 (2020) https://doi.org/10.4271/2020-01-0792

Wu, Z., Huang, N. E.: Ensemble empirical mode decomposition: A noise-assisted data analysis method. Adv. Adapt. Data Anal. **1**(1), 1–41 (2009) https://doi.org/10.1142/S1793536909000047

Xia, Y., Zhang, B., Pei, W., Mandic, D. P.: Bidimensional multivariate empirical mode decomposition with applications in multi-scale image fusion. IEEE Access **7**, 114261–114270 (2019) https://doi.org/10.1109/ACCESS.2019.2936030

Yavuz, I., Refined turbulence models for simulation of IC-engine cylinder flows. PhD thesis, West Virginia University (2000) https://doi.org/10.33915/etd.2309

Young, M. B.: Cyclic dispersion in the homogeneous-charge spark-ignition engine—a literature survey. SAE Tech. Pap. 810020 (1981) https://doi.org/https://doi.org/10.4271/810020

Zentgraf, F., Baum, E., Böhm, B., Dreizler, A., Peterson, B.: On the turbulent flow in piston engines: Coupling of statistical theory quantities and instantaneous turbulence. Phys. Fluids **28**(4), 045108 (2016) https://doi.org/10.1063/1.4945785

Zhao, L., Moiz, A. A., Som, S., Fogla, N., Bybee, M., Wahiduzzaman, S., Mirzaeian, M., Millo, F., Kodavasal, J.: Examining the role of flame topologies and in-cylinder flow fields on cyclic variability in spark-ignited engines using large-eddy simulation. Int. J. Engine Res. **19**(8), 886–904 (2018) https://doi.org/10.1177/1468087417732447

Zivot, E., Wang, J.: Vector Autoregressive Models for Multivariate Time Series. In: Modeling Financial Time Series with S-Plus®, Springer, 369–413 (2003) https://doi.org/10.1007/978-0-387-21763-5_11